Computers and Geotechnics 159 (2023) 105400

Contents lists available at ScienceDirect

Computers and Geotechnics

journal homepage: www.elsevier.com/locate/compgeo

A new approach to model geomaterials with heterogeneous properties in thermo-hydro-mechanical coupled problems

Alfonso Rodriguez-Dono [a,b,*], Yunfeng Zhou [a], Sebastia Olivella [a,b]

[a] Department of Civil and Environmental Engineering, Universitat Politècnica de Catalunya · BarcelonaTech (UPC), Barcelona 08034, Spain
[b] International Centre for Numerical Methods in Engineering (CIMNE), Barcelona 08034, Spain

ARTICLE INFO

Keywords:
Heterogeneity
Thermo-hydro-mechanical modelling
CODE_BRIGHT
Coupled problems
Anisotropy
Porosity

ABSTRACT

The main objective of this article is to present a new approach to model coupled thermo-hydro-mechanical problems considering geomaterials with heterogeneous properties. This approach has been implemented in the software CODE_BRIGHT and it provides the possibility of considering geomaterials with a spatially correlated heterogeneous field of porosity, following a normal distribution. This spatial correlation can be isotropic or anisotropic. An important feature of this approach is that material properties such as intrinsic permeability, thermal conductivity, diffusivity, retention curve, elastic modulus or cohesion are defined as a function of porosity and, thus, they become heterogeneous with spatial correlation and, eventually, anisotropic. A validation exercise and other basic numerical examples have been carried out to illustrate the possibilities of the proposed approach. The results, which have been compared with a homogeneous case, show that considering heterogeneous fields can be relevant in different modelling problems, especially coupled thermo-hydro-mechanical problems.

1. Introduction

It is well known that geomaterials including soils, rocks and concrete are heterogeneous and, at the grain scale, are characterized by the presence of different materials (i.e., minerals) and micro-structural defects (i.e., microcracks) (Mahabadi et al., 2012). When the material is under thermo-hydro-mechanical (THM) conditions, parameters such as thermal conductivity (Wang et al., 2006), intrinsic permeability (Pakzad et al., 2018), Young's modulus (Bürgmann et al., 1994), etc. are affected by the distribution and properties of the constituent minerals and bulk density. This indicates that considering heterogeneity may be relevant when modelling the THM coupled behaviour of geomaterials, although it is usually ignored. The variables that are considered heterogeneous using our proposed approach and the relationships among them are detailed in Section 3. Nevertheless, the current approach can be extended to other parameters if theoretical or experimental evidences indicate the convenience doing it, following a similar philosophy.

On the other hand, the software CODE_BRIGHT (Olivella et al., 1996) is based on the finite element method (FEM) (Gharti et al., 2012; Zienkiewicz and Taylor, 2005; Zienkiewicz and Taylor, 2000) and has been widely used successfully to model coupled thermo-hydro-mechanical (THM) problems (Gens and Olivella, 2001; Nishimura et al., 2009; Olivella and Gens, 2005; Sánchez et al., 2012). Hence, our new approach has been implemented in this software, which already has strong capabilities in modelling coupled THM problems. The general formulation of CODE_BRIGHT is presented in Olivella et al. (1996), including the weak forms of the governing equations and explicit definitions of the resulting matrices and vectors. Olivella et al. (1996) includes explanations of how variables are specifically treated in the nodes, elements and cells.

Heterogeneity is usually considered directly for specific parameters depending on the problem, for instance: transmissivity for hydrogeological problems (Meier et al., 1998; Tan and Homsy, 1992), strength for geotechnical problems (Firouzianbandpey et al., 2014; Krishna and Katsumi, 2020), thermal conductivity for heat flow problems (Jorand et al., 2013; Popov et al., 2016; Tamayo et al., 2006). But for coupled thermo-hydro-mechanical (THM) problems is seldom introduced. Therefore, the aim of this article is presenting our new approach to model THM problems considering geomaterials with heterogeneous properties. Verification of the implemented variogram to account for spatial correlation is presented in Section 4. The validation of the approach by comparison with experimental results is presented in Section 5. Moreover, in order to illustrate the capabilities of this approach,

* Corresponding author at: Department of Civil and Environmental Engineering, Universitat Politècnica de Catalunya, Barcelona 08034, Spain.
E-mail address: alfonso.rodriguez@upc.edu (A. Rodriguez-Dono).

https://doi.org/10.1016/j.compgeo.2023.105400
Received 22 December 2022; Received in revised form 14 February 2023; Accepted 9 March 2023
Available online 28 March 2023

Nomenclature

a	range in a variogram function
a_x, a_y, a_z	range on the three axes (x, y, and z)
b	aperture of embedded fractures
b_0	initial aperture of embedded fractures
b_k	calibration coefficient in the exponential law
b_{max}	maximum aperture of embedded fractures
b_p	calibration coefficient in the capillary pressure parameter function
$c(\cdot)$	cohesion function
c_0, c_1, c_2	coefficients for calibration
$C(\cdot)$	covariance function
$C(0)$	maximum variance in a covariance function
C_0	nugget
C_1	a parameter which equals to the maximum variance minus the value of nugget C_0
$dE/d\phi$	variation of Young's modulus with porosity
D_{eff}	coefficient of effective diffusion
D_m^{air}	molecular diffusion coefficient for air dissolved in the liquid phase
D_m^{vap}	molecular diffusion coefficient for water vapor in the gas phase
e	void ratio
E_0	initial Young's modulus
$E(\cdot)$	Young's modulus function dependent on porosity, following a linear law
F	Drucker-Prager yield function
$\boldsymbol{g}$	vector of gravitational forces
G	shear modulus
G_f	flow rule
$\boldsymbol{h}$	distance vector between two elements
$\lvert\boldsymbol{h}\rvert$	distance between two elements
$\boldsymbol{i}_c$	thermal flux in Fourier's law
$\boldsymbol{i}_f$	diffusive flux of a component in a fluid
$\boldsymbol{I}$	identity matrix
$\boldsymbol{k}$	intrinsic permeability tensor
k	intrinsic permeability
k_0	intrinsic permeability for model calibrations
$k_{fracture}$	permeability corresponding to embedded fractures
k_{matrix}	intrinsic permeability for matrix of geomaterials
k_r	relative permeability
k_{rg}	gas relative permeability
k_{rl}	liquid relative permeability
K	bulk modulus
L	lower triangular matrix
m	constant power in the stress function
M	parameter in Drucker-Prager yield function
n	calibration parameter in liquid relative permeability
n_c, a, b	parameter in the cohesion function to calibrate with experimental data
$N(\cdot)$	number of experimental pairs
N_1	the number of grid points
p	mean net stress
p'	mean effective stress
P_c	capillary pressure parameter
p_f	fluid pressure
P_g	gas pressure
P_l	liquid pressure
p_{swell}	swelling pressure
q	equivalent deviatoric stress
$\boldsymbol{q}_f$	advective flux in generalized Darcy's law
R	ideal gas constant
s	suction
S_e	Effective saturation
S_f	saturation degree of the fluid
S_l	liquid saturation
S_{ls}	maximum liquid saturation
S_{rl}	residual liquid saturation
α	non-associativity parameter that ranges from 0 to 1
α, γ, β	The angle with the positive direction of the coordinate axis (counterclockwise is positive)
α_{ss}	parameter relates suction and elastic stiffness
β	parameter in Drucker-Prager yield function
$\gamma(\cdot)$	variogram function
$\gamma^*(\cdot)$	experimental variogram
Γ	fluidity parameter
ε	volumetric strain
ε_0	volumetric strain in the cubic law for calibration
$\boldsymbol{\varepsilon}^e, \boldsymbol{\varepsilon}^i$	elastic and inelastic strain tensor
$\varepsilon_v^e, \varepsilon_d^e$	elastic volumetric and deviatoric strain
κ_s	elastic stiffness for changes in suction
κ_{s0}	elastic stiffness for changes in suction at reference pressure (p_{ref})
λ	bulk thermal conductivity
λ_1	range on the y axis divided by range on the x axis
λ_2	range on the z axis divided by range on the x axis
λ_c	shape function
λ_{dry}	thermal conductivity in dry conditions
λ_g	thermal conductivity for corresponding to the gas phase
λ_l	thermal conductivity for corresponding to the liquid phase
λ_s	thermal conductivity for corresponding to the solid phase
λ_{s0}	thermal conductivity for calibration corresponding to the solid phase
λ_{sat}	thermal conductivity in saturated conditions
μ	mean
ν	Poisson's ratio
ρ_{dry}	dry density
μ_f	viscosity of fluid
ρ_f	density of fluid
ρ_s	solid density
σ	standard deviation in mathematics
$\boldsymbol{\sigma}'$	effective stress tensor
σ_x', σ_y', σ_z'	effective stress in the x, y and z axis direction
τ	coefficient of tortuosity
ϕ	porosity
ϕ_0	reference porosity
ϕ_{c0}	reference porosity in the cohesion function
ϕ'	friction angle
$\Phi(\cdot)$	stress function
ω, ω^T	vector of normally distributed numbers, transpose of the vector
∇	Hamiltonian
T	temperature
U, U^T	upper triangular matrix, transpose of the matrix
y	vector of numbers following standard normal distribution
Y	random variable corresponding to vector y
$\mathrm{z(x_i)}$, $\mathrm{z(x_i} + \mathbf{h})$	measurements at any different points

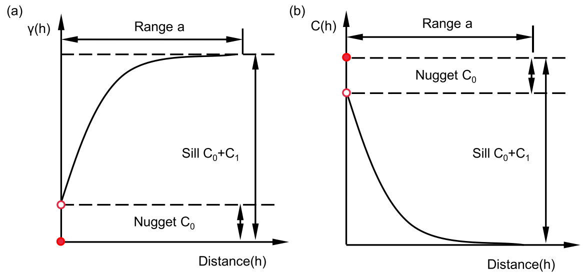

Fig. 1. Schematic representation: (a) Variogram model; (b) Covariance model.

some simple examples are presented in Section 6. The examples are motivated by current investigations in the field of radioactive waste disposal, but this is not imposing a lost of generality to the approach, which can be of interest to other applications in the field of unsaturated soil geotechnical problems, carbon injection in the underground or geothermal problems, among others.

The following sections outline a fully coupled THM FEM framework and the incorporation of the heterogeneous features to perform models intended to represent the behaviour of geomaterials as realistic as possible. Investigations have been made to evaluate the model performance. As discussed below, the present model has limitations in simulating large-scale structures. However, new algorithms could be adopted to improve the efficiency of the proposed framework.

2. Theoretical background

2.1. Geostatistics

Geostatistics offers a way of describing the spatial continuity that is an essential feature of many natural phenomena and provides adaptations of classical regression techniques to take advantage of this continuity (Isaaks et al., 1989).

Semi-variogram analysis and stochastic simulation are two basic components of geostatistics. Semi-variogram analysis is the characterization of spatial correlation, and stochastic simulation employs a semi-variogram model to generate multiple equiprobable images of the variable. The spherical semi-variogram (Eq. (1)) has been chosen as the basis for the implementation in CODE_BRIGHT (Olivella et al., 1996) since perhaps it is the most commonly used semi-variogram model (Isaaks et al., 1989; Journel and Huijbregts, 1976). In the spherical semi-variogram, C_0 is the nugget, which is due both to measurement errors and to micro-variabilities of the mineralization. a denotes the range, which means that any data value will be correlated with any other value falling within a radius a (as shown in Fig. 1).

As a function of $|\boldsymbol{h}|$, which is the distance between two elements, the spherical semi-variogram is defined as in Eq. (1).

$$\gamma(h) = \begin{cases} 0, & |\boldsymbol{h}| = 0 \\ C_0 + C_1\left[\dfrac{3}{2}\dfrac{|\boldsymbol{h}|}{a} - \dfrac{1}{2}\left(\dfrac{|\boldsymbol{h}|}{a}\right)^3\right], & 0 < |\boldsymbol{h}| \le a \\ C_0 + C_1, & |\boldsymbol{h}| > a \end{cases} \tag{1}$$

Geostatistical methods are optimal when data are normally distributed and stationary, i.e. mean and variance do not vary significantly in space (Bohling, 2005). Algorithms to simulate a Gaussian and stationary field can be classified into two categories: exact and approximate ones. The approximate algorithms are practical when the simulation domains contain millions of nodes (Emery and Lantuéjoul, 2006). In contrast, the LU decomposition of the covariance matrix (Davis, 1987) of the first family is applicable to any configuration of the simulated locations and any covariance model, although it is costly. But this depends on the size of the problem to be solved. In THM applications with highly non-linear functions meshes are relatively small and the cost of field generation is not large compared to the finite element calculation of transient problems. The 2D and 3D formulations of this approach are identical, which makes easier the implementation in CODE_BRIGHT, compared with the turning bands method (Matheron, 1973).

2.2. Heterogeneous field generation

The development of a spatially correlated heterogeneous field of porosity is based on the work of Davis (1987), following the geostatistical theory and using the LU triangular decomposition technique (Eq. (2)–(5)), where $\mathbf{C}$ is the covariance matrix of N_1 grid points to simulate, which is positive-definite and can be decomposed into upper and lower triangular matrices (Cholesky algorithm); ω is a vector of N_1 independent normally distributed random numbers. The vector $\mathbf{y}$ can be defined as in Eq. (3). Then, the mean and covariance of the random variable $\mathbf{Y}$ corresponding to $\mathbf{y}$ are obtained (Eq. (4)–(5)).

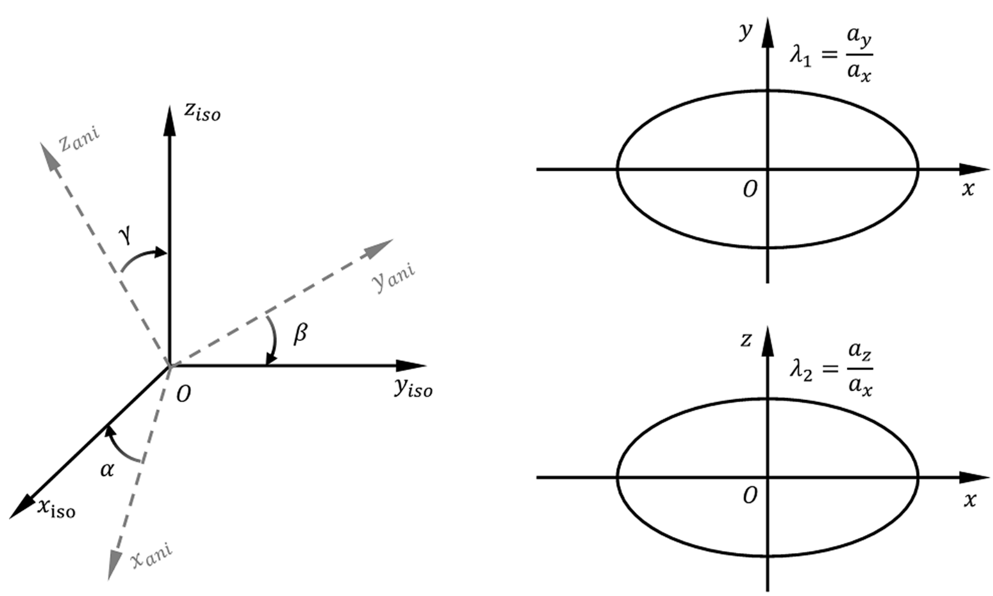

Fig. 2. An example of the five parameters needed to define the geometric anisotropy of a covariance function in 3D.

Table 1
Parameters that can be considered as a function of porosity.

Parameter	Symbol	Equations
Intrinsic permeability	k	Eqs. (17) or (19)
Thermal conductivity	λ	Eqs. (25)–(29)
Coefficient of effective diffusion	D_{eff}	Eq. (30)
Capillary pressure (Van Genuchten)	P_c	Eqs. (22) and (33)
Shape parameter (Van Genuchten)	λ_c	Eq. (33)
Young modulus	E	Eq. (35)
Cohesion	c	Eq. (44)
Swelling pressure	p_{swell}	Eq. (45)

$$\mathbf{C} = \mathbf{LU}, \text{ with } \mathbf{L} = \mathbf{U}^T \tag{2}$$

$$\mathbf{y} = \mathbf{L\omega} \tag{3}$$

$$E(\mathbf{Y}) = 0 \tag{4}$$

$$Cov(\mathbf{Y}) = E\left(\mathbf{L\omega}(\mathbf{L\omega})^T\right) = LE\left(\boldsymbol{\omega\omega}^T\right)\mathbf{U} = \mathbf{C} \tag{5}$$

Under the condition of second-order stationarity, i.e. spatially constant mean and variance (Bohling, 2005), the relationship between covariance function and semi-variogram can be given by Eq. (6). Thus, the spherical covariance model (Eq. (7)), which is consistent with Eq. (1), is adopted.

$$C(\boldsymbol{h}) = C(0) - \gamma(\boldsymbol{h}) \tag{6}$$

$$C(\boldsymbol{h}) = \begin{cases} C_0 + C_1, & |\boldsymbol{h}| = 0 \\ C_1\left[1 - 1.5\dfrac{|\boldsymbol{h}|}{a} + 0.5\left(\dfrac{|\boldsymbol{h}|}{a}\right)^3\right], & 0 < |\boldsymbol{h}| \le a \\ 0, & |\boldsymbol{h}| > a \end{cases} \tag{7}$$

Then, vector y is therefore the autocorrelated simulation with the covariance model $C(\boldsymbol{h})$. If a random field of porosity (ϕ) with mean μ and covariance $C_0 + C_1$ is generated, and the range is a, Eq. (8) can be derived. Thus, mean and covariance are given by Eq. (9).

$$\phi = y + \mu \tag{8}$$

$$E(\phi) = \mu, \qquad Cov(\phi) = C_0 + C_1 \tag{9}$$

The described phenomenon is said to be "anisotropic", when the covariance function $C(\boldsymbol{h})$ depends on both the modulus and the direction of vector $\boldsymbol{h}$ (Journel and Huijbregts, 1976). The directional graph of the range a is an ellipsoid in three dimensions. It is isotropic if the covariance function depends on the modulus of vector $\boldsymbol{h}$. There are two main types of anisotropy. A geometric anisotropy is the one that has approximately the same sill but a different range value in different directions. A zonal anisotropy is one in which the sill value changes with direction while the range remains constant (Isaaks et al., 1989). The latter type can be considered as a particular case of the former one (Deutsch and Journel, 1992), so the geometric anisotropy is introduced in detail.

Two steps are taken to obtain the anisotropic covariance function since the isotropic one has been already shown in Eq. (7), which means transforming an ellipsoid into a sphere. The first step is to rotate the coordinate axes by the angles α, β, and γ (Fig. 2), so that they become parallel to the main axes of the ellipsoid. Then, the new coordinates are represented by Eq. (10), where coordinates with subscripts "ani" are the original ones. Matrix $[R]$ (Eq. (11)), from left to right, contains the rotations around the axis x, y and z.

$$\begin{bmatrix} x_{ani1} \\ y_{ani1} \\ z_{ani1} \end{bmatrix} = [\mathrm{R}] \begin{bmatrix} x_{ani} \\ y_{ani} \\ z_{ani} \end{bmatrix} \tag{10}$$

$$with\ [\mathrm{R}] = \begin{bmatrix} 1 & 0 & 0 \\ 0 & \cos(\beta) & \sin(\beta) \\ 0 & -\sin(\beta) & \cos(\beta) \end{bmatrix} \begin{bmatrix} \cos(\gamma) & 0 & \sin(\gamma) \\ 0 & 1 & 0 \\ -\sin(\gamma) & 0 & \cos(\gamma) \end{bmatrix} \begin{bmatrix} \cos(\alpha) & \sin(\alpha) & 0 \\ -\sin(\alpha) & \cos(\alpha) & 0 \\ 0 & 0 & 1 \end{bmatrix} \tag{11}$$

Next step is to transform the ellipsoid into a sphere with a radius equal to the major range a_x (shown in Fig. 2) of the ellipsoid. This is achieved by multiplying the coordinate in step one by the ratio of anisotropy matrix (Eq. (12)), where $\lambda_1 = a_y/a_x$, $\lambda_2 = a_z/a_x$, a_x, a_y, and a_z are ranges for axis x, y, and z, respectively;

$$\begin{bmatrix} x_{iso} \\ y_{iso} \\ z_{iso} \end{bmatrix} = [\lambda][\mathrm{R}] \begin{bmatrix} x_{ani} \\ y_{ani} \\ z_{ani} \end{bmatrix}, \qquad \text{with}[\lambda] = \begin{bmatrix} 1 \\ \lambda_1 \\ \lambda_2 \end{bmatrix} \tag{12}$$

3. Proposed approach for generating heterogeneous fields

Many parameters in CODE_BRIGHT can be a function of porosity, which means heterogeneous features are inherited automatically (a summary is presented in Table 1 and each of the parameters will be explained below). In addition, it was found that the pore size distribution of some rocks (e.g. COx, a clay rock), approximately follow a normal distribution (Armand et al., 2017). These reasons led to the selection of porosity as the variable used to generate a spatially correlated field following a normal distribution.

As indicated above, the proposed approach has been implemented in the finite element method (FEM) software CODE_BRIGHT (Olivella et al., 1996). CODE_BRIGHT has been developed by the Department of Civil and Environmental Engineering of the Universitat Politècnica de Catalunya (UPC), and works in combination with the pre/post-processor GID (Coll et al., 2018), developed by the International Centre for Numerical Methods in Engineering (CIMNE). A detailed description of the numerical approach employed in CODE_BRIGHT can be found in the work of Olivella et al. (1996) and Olivella (1995).

3.1. Heterogeneous field of porosity

Following the theory exposed in Section 2.2, a specific module has been developed in CODE_BRIGHT to generate a spatially correlated heterogeneous field of porosity, following a Gaussian random distribution of mean μ and standard deviation σ (square root of the variance) (Fig. 3a). In the practical use of the approach, only values of the distribution between $\mu - 3\sigma$ and $\mu + 3\sigma$ are considered, to avoid numerical difficulties related to outliers. In the field of contaminant transport (Alabert, 1987) and geotechnics (Firouzianbandpey et al., 2014), the types of correlation function and range parameters are determined by curve fitting of semi-variograms.

On the sample scale, these semi-variograms can be obtain using different techniques. For example, Sammartino et al. (2002) used a microstructural imaging technique, the ^{14}C-PolyMethylMethAcrylate (PMMA) method, to map and quantify the porosity of sedimentary rocks. Wu et al. (2004) described a method for determine the heterogeneity of soil properties from porosity maps, and obtained semi-variograms of porosity spatial distribution in different samples. These maps are drawn from physical information from the micrometer to the decimeter scale. In addition, Focused Ion Beam/Scanning Electron Microscopy (FIB/SEM), and Transmission Electron Microscopy (TEM) can provide complementary information about the pore network connectivity, anisotropy, tortuosity of geomaterials, etc. (Song et al., 2015).

The aforementioned techniques can be used to characterize samples and to simulate laboratory experiments, assuming that the sample is heterogeneous. The same techniques can be used in a field scale provided that several samples at different locations are available. For

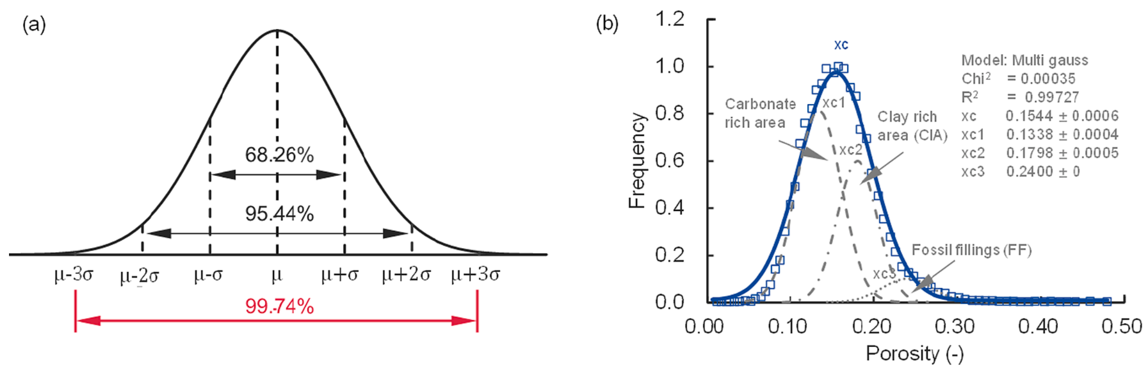

Fig. 3. Normal porosity distribution: (a) Schematic diagram of the probability density curve; (b) Porosity histogram of a claystone, according to Sammartino et al. (2002) and modified from Géraud et al. (2007).

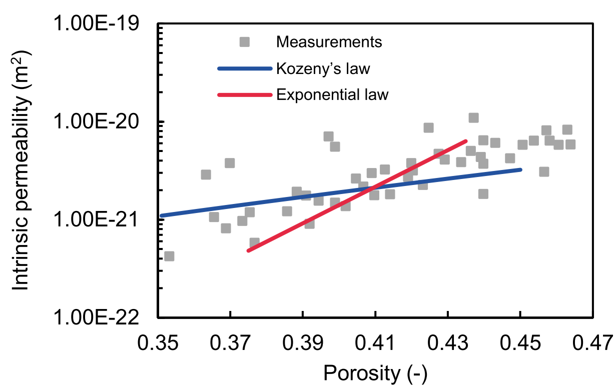

Fig. 4. Experimental data corresponding to bentonite and adopted models for the intrinsic permeability law, modified from Sánchez et al. (2012). Note that the slope of the exponential law can be adjusted while Kozeny has no parameter to allow adjustment.

example, Yven et al. (2007) combined imaging techniques and borehole measurements to determine the spatial variability of the porosity at the field scale. Another approach is to determine semi-variograms from dry density measurements in samples (Toprak et al., 2018) or in-situ experiments (Rodriguez-Dono et al., 2018).

Thus, using different techniques, the basic parameters (covariance, mean, range, rotation angle) for the semi-variograms can be estimated and, hence, the anisotropic heterogeneous field is generated by the proposed approach aforementioned in Section 2.2.

3.2. Heterogeneous field of permeability

The advective flux $\mathbf{q}_f$ related to fluid motion is governed by the generalised Darcy's law, as shown in Eq. (13), where $\mathbf{k}$ represents the intrinsic permeability tensor; k_r represents the relative permeability; p_f is the fluid pressure; ρ_f and μ_f are the density and the viscosity of the fluid; and $\mathbf{g}$ represents the vector of gravitational forces.(13)

$$\mathbf{q}_f = -\frac{\mathbf{k}k_r}{\mu_f}(\nabla p_f - \rho_f \mathbf{g}) \tag{13}$$

In modelling complex fluid injection problems, intrinsic permeability can be considered as the sum of two terms (Eq. (14)). The first one (k_{matrix}) is a function of the porosity ϕ of the matrix of the material according to Kozeny's law (Eq. (15); Fig. 4). The second term ($k_{fracture}$) corresponds to the permeability associated with the aperture b of embedded fractures, according to a cubic law (Eq. (16)) (Lee and Cho, 2002; Olsson and Barton, 2001; Olivella and Alonso, 2008). These small micro-fractures or openings may develop in the material leading to preferential flow paths. Thus, this approach permits differentiating between the intrinsic permeability associated with the matrix and with the fractures (Damians et al., 2020). Eq. (17) can be obtained combining Eq. (15) and Eq. (16), where k_0 represents the intrinsic permeability corresponding to a reference porosity ϕ_0 of the matrix; and s is the spacing among fractures. The aperture b is calculated as shown in Eq. (18), where ε and ε_0 refer to strain (with $\varepsilon > 0$ meaning extension), and b_0 and b_{max} are the initial and maximum apertures, respectively. Note that in the case of rock masses with low porosity, the first term (k_{matrix}) can be neglected and thus, their intrinsic permeability is mainly due to fractures.

$$k = k_{matrix} + k_{fracture} \tag{14}$$

$$k_{matrix} = \frac{k_0(1-\phi_0)^2}{\phi_0^3}\frac{\phi^3}{(1-\phi)^2} \tag{15}$$

$$k_{fracture} = \frac{b^3}{12s} \tag{16}$$

$$k = \frac{k_0(1-\phi_0)^2}{\phi_0^3}\frac{\phi^3}{(1-\phi)^2} + \frac{b^3}{12s} \tag{17}$$

$$b = b_0 + (\varepsilon - \varepsilon_0)s \leq b_{max} \tag{18}$$

Nevertheless, intrinsic permeability can also be modelled using an exponential law (Fig. 4), as in Eq. (19), where b_k is a calibration coefficient. Note that exponential law has been found to represent more accurately the intrinsic permeability of some geomaterials (e.g. bentonite). Furthermore, capillary pressure parameter P_c (in retention curve; see Section 3.5) can be considered a function of intrinsic permeability k, as shown in Eq. (20). Combining Eq. (19) and Eq. (20), as shown in Eq. (21), we can obtain Eq. (22), where retention curve and intrinsic permeability parameters are related by $b_P = b_k/3$.

$$k = k_0 exp(b_k(\phi - \phi_0)) \tag{19}$$

$$\frac{P_c}{p_0} = \left(\frac{k_0}{k}\right)^{\frac{1}{3}} \tag{20}$$

$$\frac{P_c}{p_0} = \left(\frac{k_0}{k_0 \exp(b_k(\phi-\phi_0))}\right)^{\frac{1}{3}} = \exp\left(\frac{-b_k}{3}(\phi-\phi_0)\right) = \exp(b_P(\phi_0-\phi)) \tag{21}$$

$$P_c = P_0 \exp(b_P(\phi_0 - \phi)) \tag{22}$$

Regarding relative permeability, various functions can be used to describe the dependence of liquid relative permeability on the degree of saturation, for instance Eq. (23), where S_l, S_{rl} and S_{ls} are liquid saturation, residual liquid saturation and maximum liquid saturation, respectively; n is a calibration parameter that can be determined from

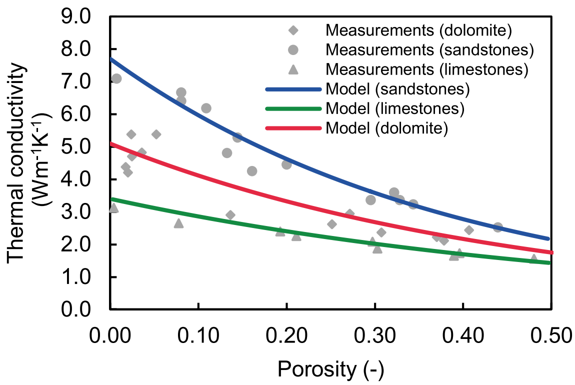

Fig. 5. Experimental data (taken from Brigaud and Vasseur (1989) and adopted model for thermal conductivity of different sedimentary rocks.

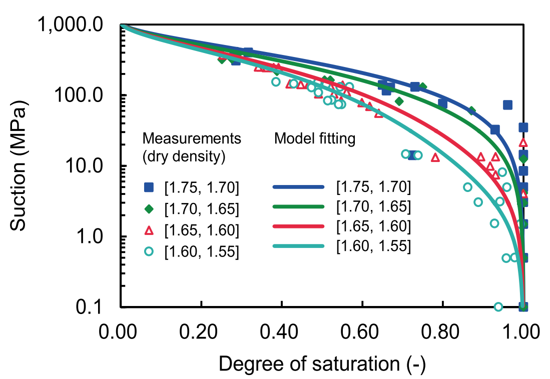

Fig. 6. Fitted retention curves and experimental data for bentonite with different initial dry densities (Gens et al., 2009).

back-calculating hydration tests. On the other hand, the gas relative permeability is a function of liquid relative permeability (Eq. (24)).

$$k_{rl} = S_e^n, \qquad with\ S_e = \frac{S_l - S_{rl}}{S_{ls} - S_{rl}} \tag{23}$$

$$k_{rg} = 1 - k_{rl} \tag{24}$$

Without loss of generality, different relative permeability can be used for fractures and matrix (see Damians et al., 2020). Nonetheless, in case of using a double structure model, this method can be used to generate a macroporosity field, which in turn controls the intrinsic permeability (T8). In this type of approaches, the microporosity plays a role on fluid accumulation (for the representation of swelling of clay aggregates at the microscale).

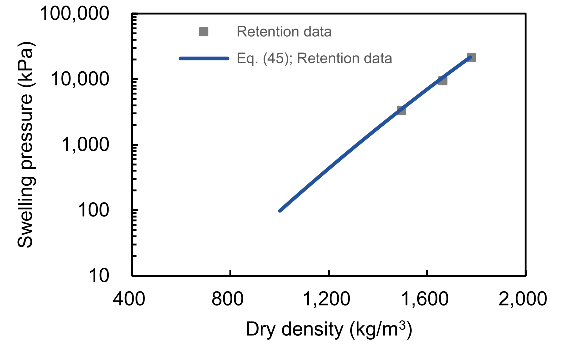

Fig. 8. Swelling pressure as a function of dry density, following Eq. (45) with $c_0 = -1.741$, $c_1 = 4.117 \times 10^{-3}$ and $c_2 = -3.94 \times 10^{-7}$ (Åkesson et al., 2010; Dueck, 2004).

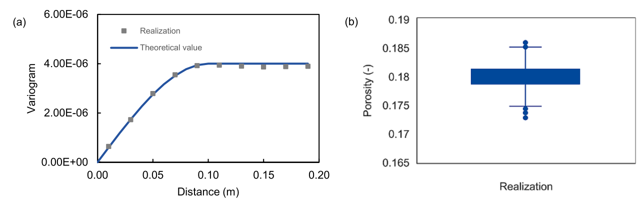

Fig. 9. (a) Variogram of a realization and the theoretical curve of the spherical variogram function with $C_0 = 0$, $C_1 = 4.00 \times 10^{-6}$, $a = 0.1$ m; (b) Box-plot computed from the isotropic heterogeneous porosity field with a spherical variogram function.

Finally, note that Eq. (15) can be rewritten as $k = k_0 \left(\frac{\phi}{\phi_0}\right)^3 \left(\frac{1-\phi_0}{1-\phi}\right)^2$. If ϕ_0 is smaller than 1–2 %, e.g. in geomaterials like coal (Wu et al., 2010), the third term $\left(\frac{1-\phi_0}{1-\phi}\right)^2$ approaches 1. Therefore, $k = k_0 \left(\frac{\phi}{\phi_0}\right)^3$ is obtained.

3.3. Heterogeneous field of thermal conductivity

Thermal conductivity is used in Fourier's law to compute conductive heat flux (Eq. (25)). There are two possibilities to calculate thermal conductivity in CODE_BRIGHT:

a) By using the thermal conductivity at dry (λ_{dry}) and saturated (λ_{sat}) conditions, as shown in Eq. (26), where S_l is the liquid saturation degree. These values at dry and saturated conditions can be measured in the laboratory.

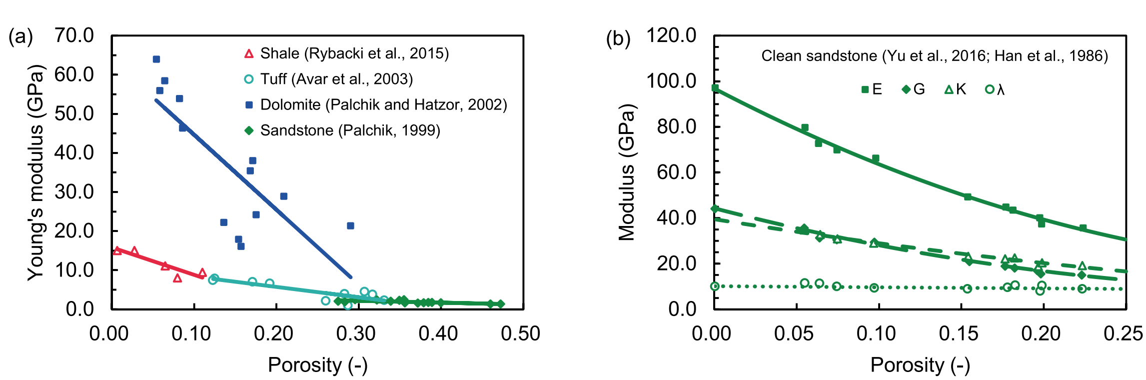

Fig. 7. (a) Young's modulus as a function of porosity for different kinds of geomaterials: shale (Rybacki et al., 2015), tuff (Avar et al., 2003), dolomite (Palchik and Hatzor, 2002), and sandstone (Palchik, 1999); (b) Different kinds of modulus for clean sandstone (Han et al., 1986; Yu et al., 2016); *E*, *G*, *K*, and λ are Young's modulus, shear modulus, bulk modulus, and Lame parameter, respectively. Symbols in the figures are measurements, and lines are fittings.

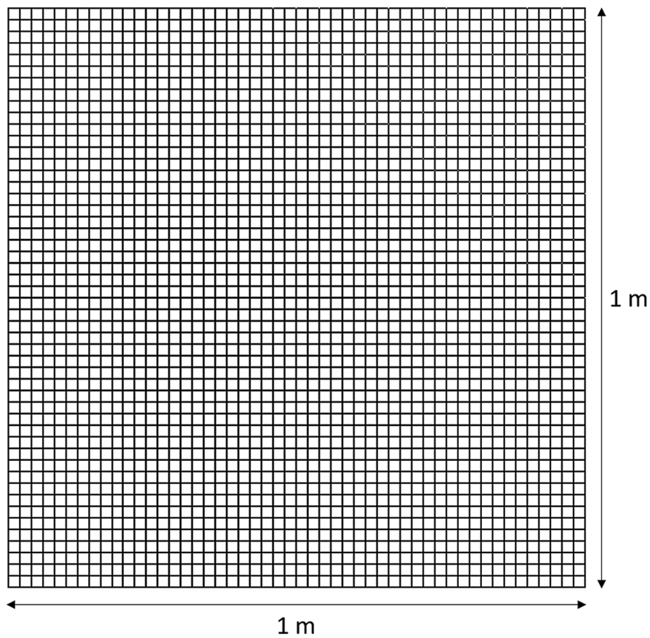

Fig. 10. Model geometry and regular mesh of quadrilateral elements of dimensions $0.02 \times 0.02\text{m}^2$.

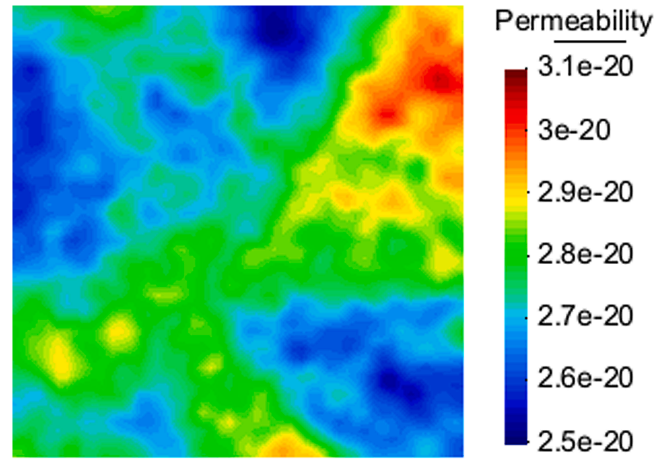

Fig. 12. Heterogeneous permeability distribution resulting from the heterogeneous porosity distribution.

b) By using the thermal conductivity of the different phases of the medium, i.e. the thermal conductivity corresponding to the solid phase λ_{s0}, the liquid phase λ_l and the gas phase λ_g, as well as the parameters a_1, a_2 and a_3 corresponding to Eq. (27). In this case, λ_{dry} and λ_{sat} can be calculated according to Eq. (28)–(29).

$$\mathbf{i}_c = -\lambda \nabla T \tag{25}$$

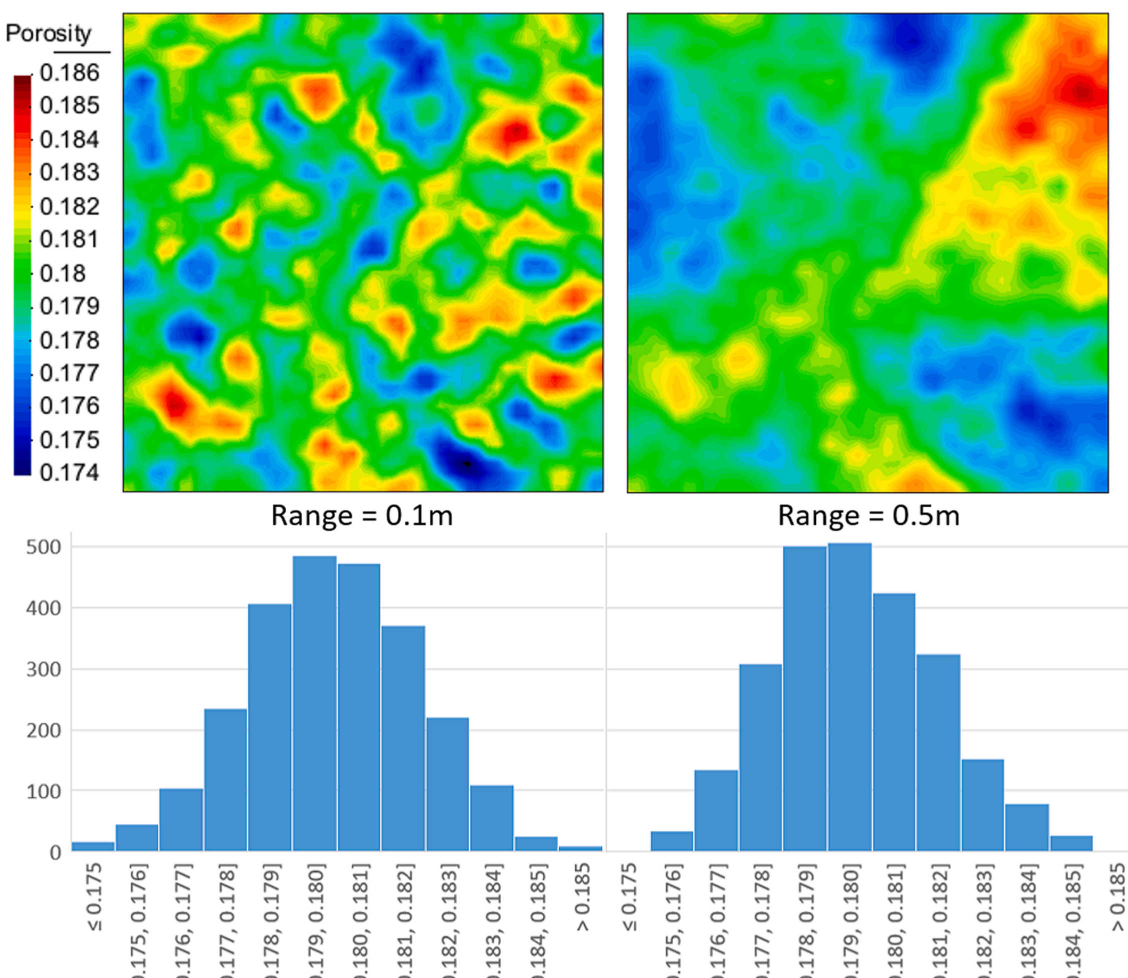

Fig. 11. Influence of the range value in spatial correlation and porosity distribution.

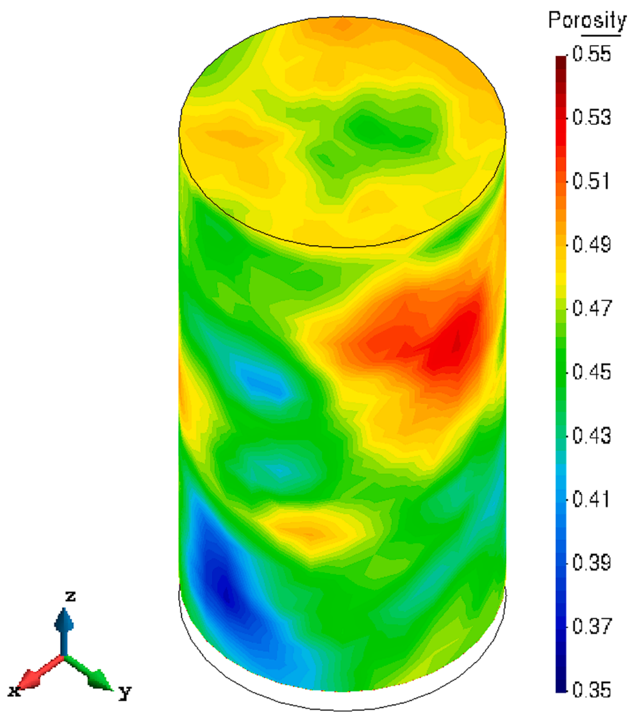

Fig. 13. Geometry of the model and initial porosity distribution assumed for the bentonite in one of the models (heterogeneous seed 2).

Table 2
Hydraulic parameters for the 3D gas injection model.

Water retention curve		Intrinsic permeability (Darcy's law):			
		Exponential:		Cubic law:	
P_0 : MPa	22.5	k_0 : m^2	3.3×10^{-21}	s : m	4×10^{-5}
ϕ_0	0.45	ϕ_0	0.45	b_0/b_{max} : m	$5 \times 10^{-9}/5 \times 10^{-7}$
b_P	12	b_k	36	ε_0	1×10^{-4}

$$\lambda = \lambda_{sat}^{S_l} \lambda_{dry}^{1-S_l} \tag{26}$$

$$\lambda_s = \lambda_{s0} + a_1 T + a_2 T^2 + a_3 T^3 \tag{27}$$

$$\lambda_{dry} = \lambda_s^{1-\phi} \lambda_g^{\phi} \tag{28}$$

$$\lambda_{sat} = \lambda_s^{1-\phi} \lambda_l^{\phi} \tag{29}$$

Although the geometric mean has been chosen in the case of Eq. (25)–(29), other equations based on arithmetic or harmonic averages or even empirical equations of the thermal conductivity as a function of porosity could be used if it was deemed more adequate (Olivella et al., 2022).

From the experimental side, Fig. 5 clearly indicates that there is a dependency of the thermal conductivity on porosity. Lower porosity will result in higher thermal conductivity. Therefore, a heterogeneous distribution of porosity will result in a heterogeneous distribution of thermal conductivity.

3.4. Heterogeneous field of diffusivity

Diffusion is a process modelled using Fick's law (Eq. (30)), where $\mathbf{i}_f$ is the diffusive flux of a component in a fluid, ϕ is porosity, ρ_f is the density of the fluid, S_f is the saturation degree of the fluid, τ is the coefficient of tortuosity, D_m is the molecular diffusion coefficient and ω_f is the mass fraction of the component in the fluid. It can be applied for example to water vapour or to dissolved air. Note $\mathbf{I}$ is the identity matrix and D_{eff} is the coefficient of effective diffusion. In the case of molecular diffusion of water vapour in the gas phase, the corresponding molecular diffusion coefficient D_m^{vap} can be calculated as in Eq. (31). In the case of air dissolved in the liquid phase, the corresponding molecular diffusion coefficient D_m^{air} can be calculated as in Eq. (32), where T is temperature in °C, P_g is the gas pressure, and $D^{vap} = 5.9 \times 10^{-6} m^2 s^{-1} K^{-n} Pa$, $D^{air} = 1.1 \times 10^{-4} m^2 s^{-1}$, $Q = 24530\,J\,mol^{-1}$ and $n_d = 2.3$. R is the ideal gas constant ($8.314\,J\,K^{-1}\,mol^{-1}$). For more details, the reader is referred to Olivella (1995).

$$\mathbf{i}_f = -(\phi \rho_f S_f \tau D_m \mathbf{I}) \nabla \omega_f = -(D_{eff} \mathbf{I}) \nabla \omega_f \tag{30}$$

$$D_m^{vap} = \frac{D^{vap}(T + 273.15)^{n_d}}{P_g} \tag{31}$$

$$D_m^{air} = D^{air} exp\left[\frac{-Q}{R(T + 273.15)}\right] \tag{32}$$

As it can be observed, the diffusive flux $\mathbf{i}_f$ depends on porosity. Therefore, a heterogeneous distribution of porosity will result in a heterogeneous distribution of diffusivity. On the other hand, as indicated in Eq. (30)–(32), the coefficient of effective diffusion depends on temperature, gas pressure, saturation, porosity and tortuosity. Tortuosity is usually considered constant and it can be used as a calibration parameter. With constant tortuosity, the equivalent diffusivity depends linearly with porosity ϕ. Moreover, a porosity function for tortuosity would lead to an equivalent diffusivity with a non-linear dependency with porosity. Accordingly, the coefficient of effective diffusion can undergo variations in space and time.

3.5. Heterogeneous field of retention curves

The retention curve is defined by Eq. (33), where P_g, P_l are the gas and liquid pressures according to Van Genuchten's (1980) model; λ_c is a shape function, which can be a function of porosity; λ_{c0} and b_{λ_c} are material parameters. As indicated before, capillary pressure parameter P_c can be considered as a function of porosity, as previously shown in Eq. (22). These functions permit calibration with experimental data in a wide variation range.

$$S_e = \left(1 + \left(\frac{P_g - P_l}{P_c}\right)^{\frac{1}{1-\lambda_c}}\right)^{-\lambda_c}$$
$$\text{with} \quad P_c = P_0 \exp(b_P(\phi_0 - \phi)) \quad \text{and} \quad \lambda_c = \lambda_{c0} \exp(b_{\lambda_c}(\phi_0 - \phi)) \tag{33}$$

Hence, since both P_c and λ_c depend on porosity, the retention curve varies with porosity. Therefore, a heterogeneous distribution of porosity will result in a heterogeneous distribution of retention curves.

Fig. 6 displays different retention curves for bentonite with different dry densities which are functions of porosity (Eq. (34)), where ρ_{dry} is the dry density, ρ_s denotes solid density and e is the void ratio as a function of porosity ϕ.

$$\rho_{dry} = \frac{\rho_s}{1 + e} \quad \text{with} \quad e = \frac{\phi}{1 - \phi} \tag{34}$$

Note that different porosities give different retention curves according to the experimental data and, thus, a heterogeneous porosity distribution will result in a distribution of retention curves along the model.

3.6. Heterogeneous mechanical properties

Regarding the elasticity of a geomaterial, the experimental work of different authors (Avar et al., 2003; Han et al., 1986; Palchik, 1999; Palchik and Hatzor, 2002; Rybacki et al., 2015; Yu et al., 2016) shows a

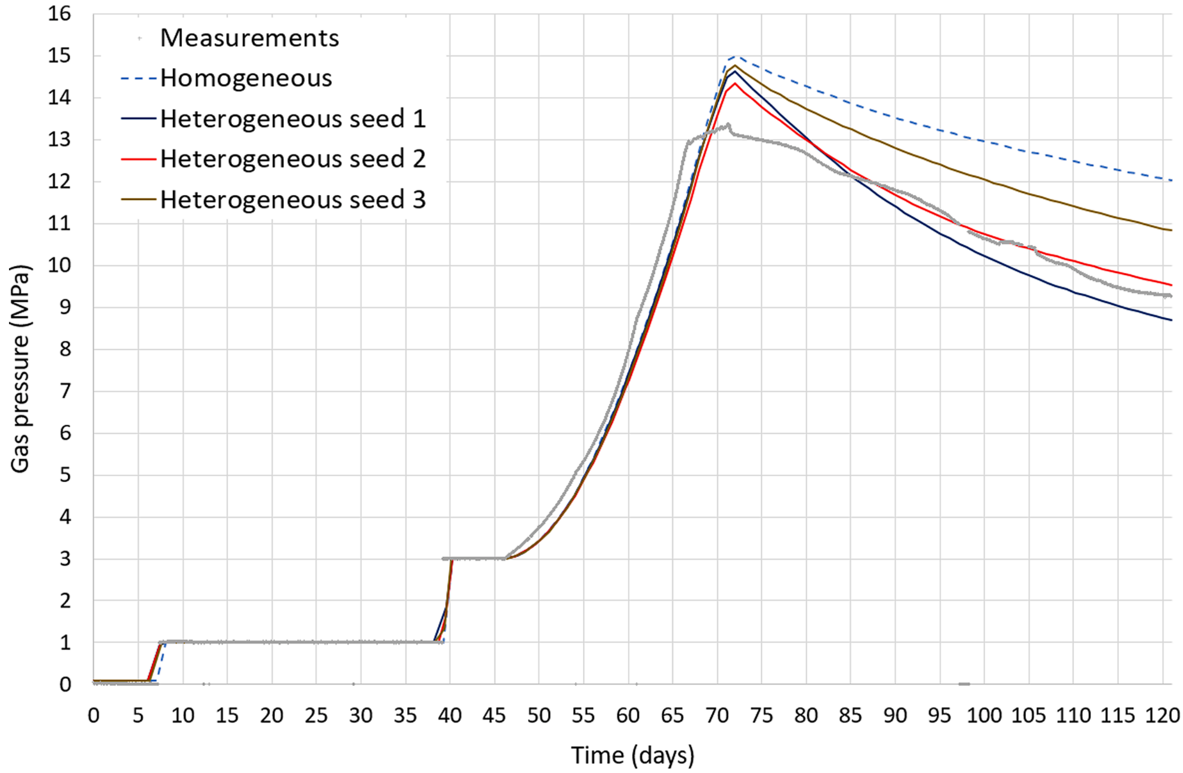

Fig. 14. 3D gas injection test. Evolution of the gas injection pressure in the different cases.

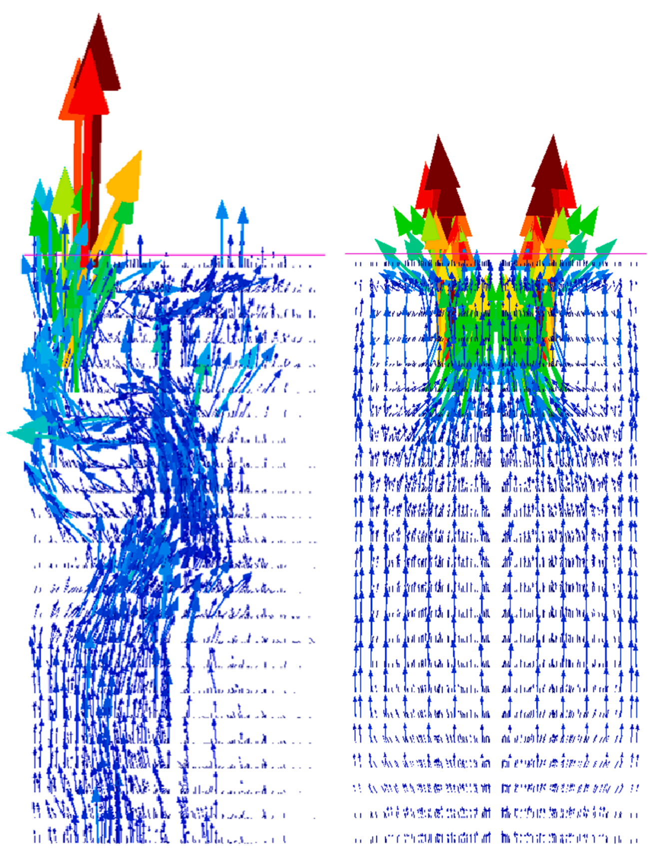

Fig. 15. 3D gas injection test. Gas path in the heterogeneous (left) and homogeneous (right) cases.

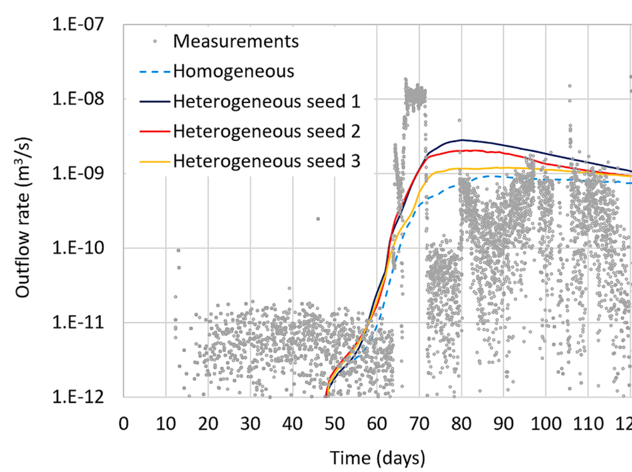

Fig. 16. 3D gas injection test. Evolution of the outflow rate in the different cases.

correlation between elastic moduli and porosity (Fig. 7), at least for some rocks. Therefore, it can be considered that the Young's modulus dependent on porosity $E(\phi)$ follows a linear law (Eq. (35)), where E_0 is the initial Young's modulus, ϕ and ϕ_0 are porosity and reference porosity, respectively; $dE/d\phi$ is the variation of Young's modulus with porosity.

$$E(\phi) = E_0 + (\phi - \phi_0)\frac{\mathrm{d}E}{d\phi} \tag{35}$$

The approach of Eq. (35) may be useful to represent monotonic loading processes, as irreversibility is not well represented. On the other hand, some models use internal variables linked to deformation e.g. hardening/softening as a function of accumulated plastic strain (Alejano et al., 2009; Mánica Malcom, 2018; Song and Rodriguez-Dono, 2021;

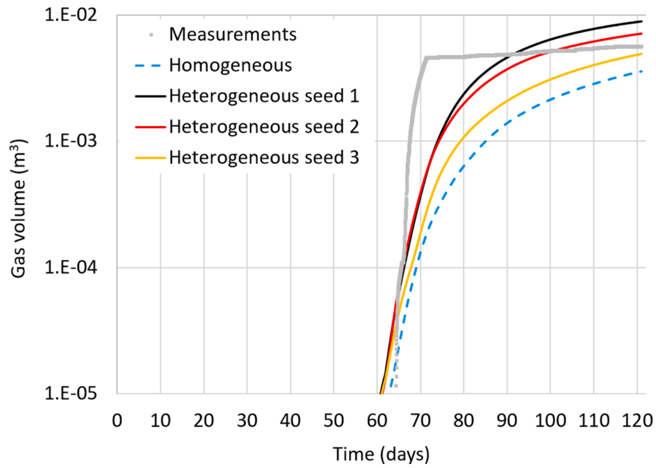

Fig. 17. 3D gas injection test. Evolution of the gas volume dissipated in the different cases.

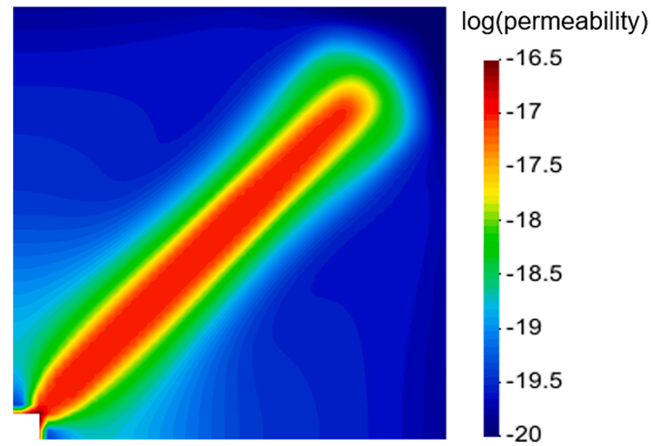

Fig. 18. 2D Gas injection test. Homogeneous case. Permeability distribution at 1000 h.

Table 3
Mechanical properties for the 2D gas injection model.

Elasticity		Visco-plasticity	
E : MPa	5240	a : MPa	5
υ	0.3	b	0
		n_c	10
		ϕ_{c0}	0.19
		M	1.3

Song et al., 2021; Song et al., 2020). The total strain can be decomposed into two parts (Eq. (36)), where ε^e is the elastic strain tensor and ε^i is the inelastic strain tensor. The elastic strain increments can be a combination of a volumetric strain (Eq. (37)) and a deviatoric strain (Eq. (38)), where ε_v^e and ε_d^e are the elastic volumetric strain and elastic deviatoric strain, respectively, $K = E/(3(1-2\nu))$ is the bulk modulus, $G = E/(2(1+\nu))$ is the shear modulus, and ν is the Poisson's ratio. (36)

$$d\boldsymbol{\varepsilon} = d\boldsymbol{\varepsilon}^e + d\boldsymbol{\varepsilon}^i \tag{36}$$

$$d\varepsilon_v^e = \frac{dp'}{K} \tag{37}$$

$$d\varepsilon_d^e = \frac{dq}{3G} \tag{38}$$

Using the viscoplastic model (Song et al., 2020), a Drucker-Prager yield function can be adopted (Eq. (39)), where q is the equivalent deviatoric stress, $p' = (\sigma_x' + \sigma_y' + \sigma_z')/3$ is the mean effective stress, c is the cohesion; M and β are parameters that can be given in compression (Eq. (40)) and extension (Eq. (41)) conditions, where ϕ' is the friction angle.

$$F = q - Mp' - c\beta \tag{39}$$

$$M = \frac{6sin\phi'}{3 - sin\phi'}, \quad \beta = \frac{6cos\phi'}{3 - sin\phi'} \tag{40}$$

$$M = \frac{6sin\phi'}{3 + sin\phi'}, \quad \beta = \frac{6cos\phi'}{3 + sin\phi'} \tag{41}$$

$F < 0$ represents the elastic stress state, and $F \geq 0$ denotes the viscoplastic behaviour, which is given by Eq. (42), where t is time, Γ is a fluidity parameter, $\Phi(F) = F^m$ is a stress function with a constant power m, $\boldsymbol{\sigma}'$ is the effective stress tensor and G_f is the flow rule, which is defined as in Eq. (43), where α is a non-associativity parameter that ranges from 0 to 1.

$$\frac{d\boldsymbol{\varepsilon}^i}{\mathrm{dt}} = \Gamma\langle\Phi(F)\rangle\frac{\partial G_f}{\partial\boldsymbol{\sigma}'} \tag{42}$$

$$G_f = q - \alpha(Mp' + c\beta) \tag{43}$$

However, how to know the accumulated plastic strain in a sample before it is tested is an issue that remains unsolved, i.e. we can measure the strain testing a sample in the lab, but we cannot measure the strain that the sample suffered historically before the test. This could justify the introduction of porosity as a measure of the internal structure of the material, since porosity can be measured independently of the history of the material. In fact, creep laws in which deformation is a function of void ratio have a consistent theoretical justification (Olivella and Gens, 2002).

In the context of crack formation by desiccation, the cohesion c has been considered a function of porosity (Trabelsi et al., 2012), as shown in Eq. (44), where ϕ_{c0} is a reference porosity and n_c, a, b are parameters to calibrate with experimental data for a particular geomaterial.

$$c(\phi) = \frac{(a + bs)(f(\phi) + |f(\phi)|)}{2} \quad \text{with} \quad f(\phi) = 1 - \left(\frac{\phi}{\phi_{c0}}\right)^{n_c} \tag{44}$$

Hence, the elastic-viscoplastic model inherits heterogeneous properties from the heterogeneous porosity distribution when Eq. (35) and Eq. (44) are incorporated. Thus, cohesion as a function of porosity may be useful to represent fractures or weakness zones, meanwhile the

Table 4
Hydraulic parameters for the 2D gas injection model.

Water retention curve (van Genuchten):		Intrinsic permeability (Darcy's law): Kozeny's model:		Cubic law:		Fick's law	
P_0 : MPa	15	k_0 : m^2	1×10^{-20}	s : m	1×10^{-5}	τ	0.25
n	0.33	ϕ_0	0.18	b_0/b_{max} : m	$1 \times 10^{-9}/1 \times 10^{-7}$		
S_{ls}/S_{rl}	1.0/0.0			ε_0	1×10^{-4}		

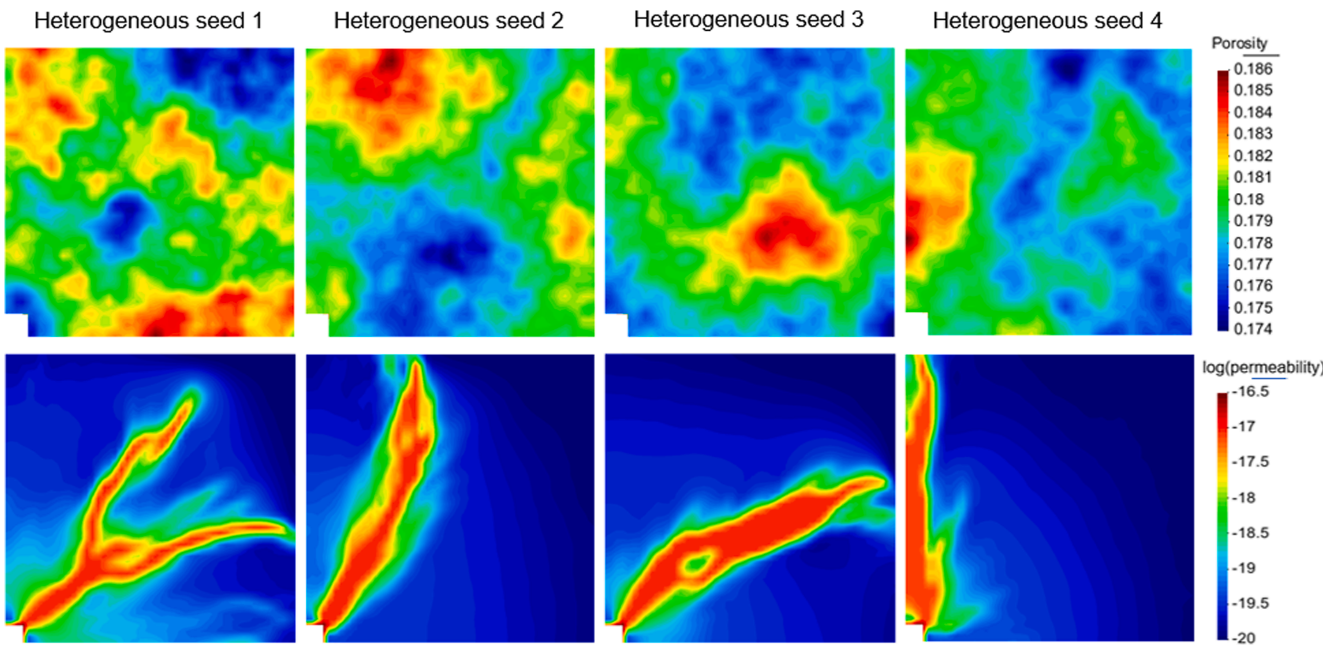

Fig. 19. 2D gas injection test. Heterogeneous cases with the same average, variance and range but with different seeds. Permeability distribution at 1000 h.

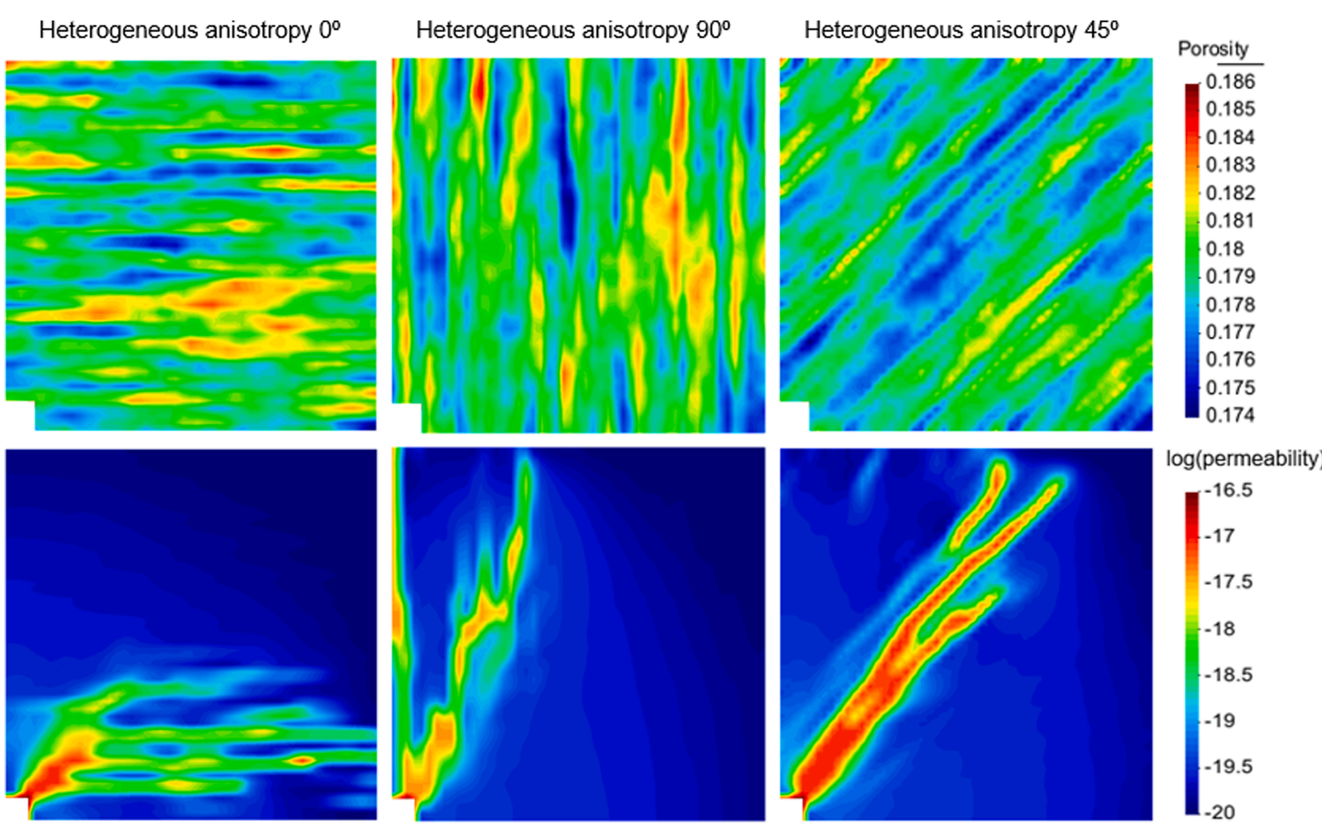

Fig. 20. 2D gas injection test. Heterogeneous anisotropic cases with the same average, variance and range but with different angles of anisotropy. Permeability distribution at 1000 h.

friction value can be kept close to the original. Note that cohesion would be variable in both space and time, following this approach. Furthermore, note that experimental results have shown that an elastic-viscoplastic approach is more adequate than an elastic–plastic approach to reproduce the yielding behaviour of geomaterials (Olivella, 1995). In addition, the viscoplastic approach facilitates the control of the size of the localised area and, therefore, avoids dependence on the mesh used (Alonso et al., 2005; Mánica Malcom, 2018; Song et al., 2020). The elastic-viscoplastic model has been frequently applied to reproduce the time-dependent effect of geomaterials (Mánica Malcom, 2018).

In the context of swelling materials, measurements of the swelling

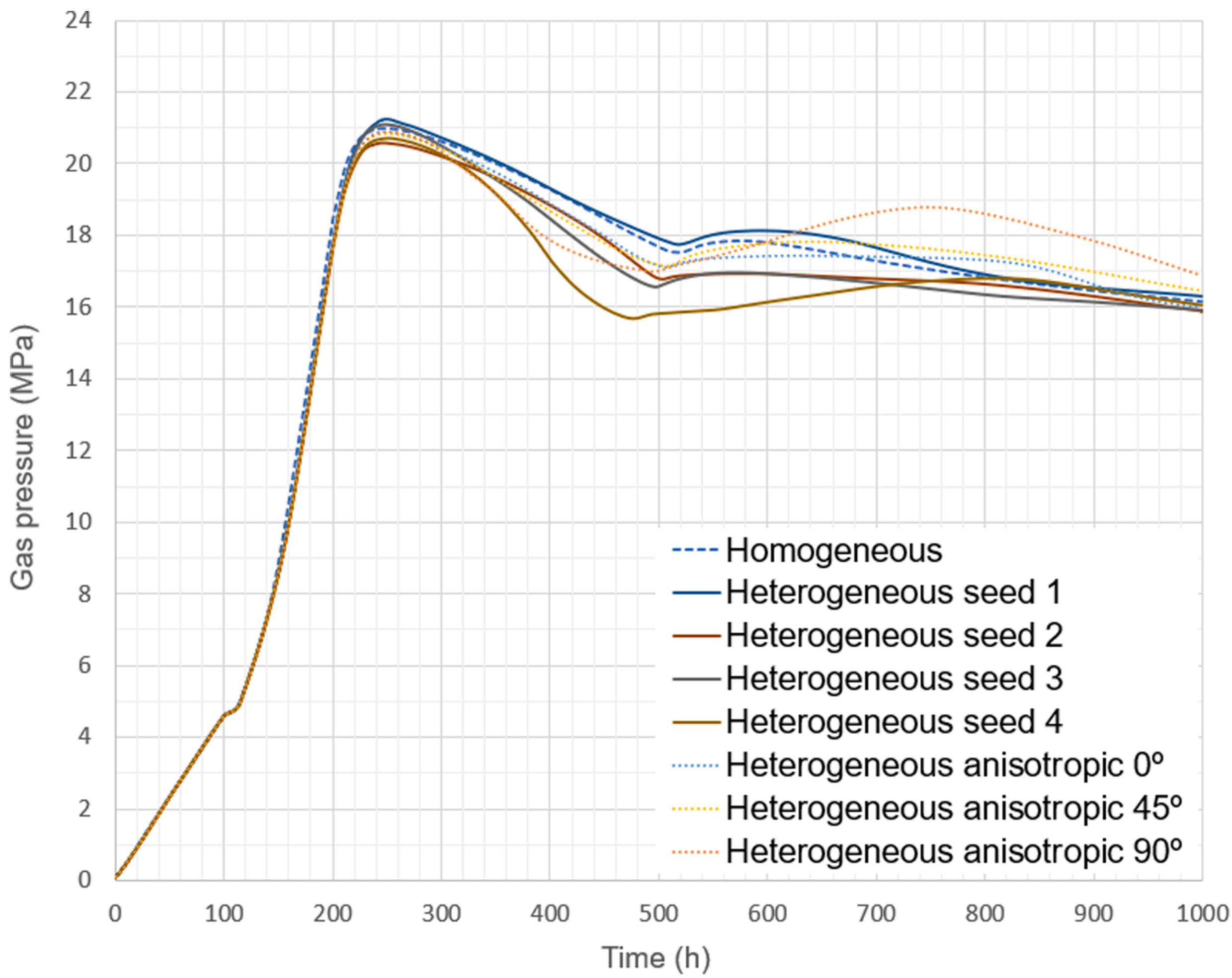

Fig. 21. 2D gas injection test. Evolution of the gas injection pressure in the different cases.

pressure (p_{swell}) at different dry densities on clay-based geomaterials that experiment swelling when hydrated were perform (Börgesson et al., 1995; Dueck, 2004; Karnland et al., 2006), showing that there is a dependence of swelling pressure (p_{swell}) on dry density (Fig. 8) and, hence, on porosity (Eq. (34)).

To account for that, it has been implemented in CODE_BRIGHT a polynomial function of the form of Eq. (45), where c_0, c_1 and c_2 are coefficients for calibration (Åkesson et al., 2010).

$$p_{swell}(\mathrm{MPa}) = \frac{10^{c_0+c_1\rho_{dry}+c_2\rho_{dry}^2}}{1000} \tag{45}$$

To improve the swelling pressure calibration in unsaturated soil modelling, swelling pressure is used to modify a parameter in Barcelona Basic Model (Gens et al., 2009), as shown in Eq. (46), where k_s, k_{s0} are elastic stiffness coefficient for changes in suction and elastic stiffness cofficient for changes in suction at reference pressure (p_{ref}), respectively. α_{ss} is a parameter related to suction and elastic stiffness coefficient, s is suction and p is the mean net stress.

$$\kappa_s = k_{s0}\exp(\alpha_{ss}s)\ln\left(\frac{p}{p_{ref}}\right)\ln\left(\frac{p_{swell}}{p_{ref}}\right) \tag{46}$$

4. Variogram verification and range effect

Regarding the variogram verification, an experimental variogram (Journel and Huijbregts, 1976) has been defined (Eq. (47)), where $\mathrm{N}(\mathbf{h})$ is the number of experimental pairs $[\mathrm{z}(\mathrm{x_i}), \mathrm{z}(\mathrm{x_i}+\mathbf{h})]$ separated by the vector $\mathbf{h}$, and $\mathrm{z}(\mathrm{x_i})$ and $\mathrm{z}(\mathrm{x_i}+\mathbf{h})$ are measurements at any different points. Note that the variogram can be estimated from in-situ measurements.

$$\gamma^*(\mathbf{h}) = \frac{1}{2\mathrm{N}(\mathbf{h})}\sum_{i=1}^{\mathrm{N}(\mathbf{h})}[\mathrm{z}(\mathrm{x_i}) - \mathrm{z}(\mathrm{x_i}+\mathbf{h})]^2 \tag{47}$$

Several factors affect the reliability of the experimental variogram (Oliver and Webster, 2014), including the number of nodes in a range, the range value and the marginal distribution. Normally, the more nodes in a range, the greater is the accuracy of the variogram. If the range value is selected reasonably, there are sufficient estimates to reveal the form of the variogram. In addition, outliers and long upper tails in the distributions of skewed data inflate variances and distort the variogram.

Fig. 9a shows variogram and box-plot of an $1\times1\,\mathrm{m}^2$ isotropic heterogeneous field with mesh size 0.01 m. It can be observed that the realization of the LU approach fits well with the theoretical curve of the spherical variogram function. There are only six outliers and they are near the populations of interest (Fig. 9b). The skewness of this random field is -0.126, close to 0, which means the marginal distribution effect can be ignored.

Regarding the range effect analysis, using CODE_BRIGHT, a 2D model with a discretised area of $1\times1\mathrm{m}^2$ has been performed. It has been considered a heterogeneous distribution of porosity with a mean of 0.18 and a standard deviation of 0.002. A regular mesh of quadrilateral elements of dimensions $0.02\times0.02\mathrm{m}^2$ has been used (Fig. 10).

Spatial correlation is controlled by the range a (see Fig. 1). In Fig. 11 it can be observed the influence of the range value in the spatial correlation. The range should be at least twice the size of the elements (in this case,0.04m) in order to have some spatial correlation. If the range is

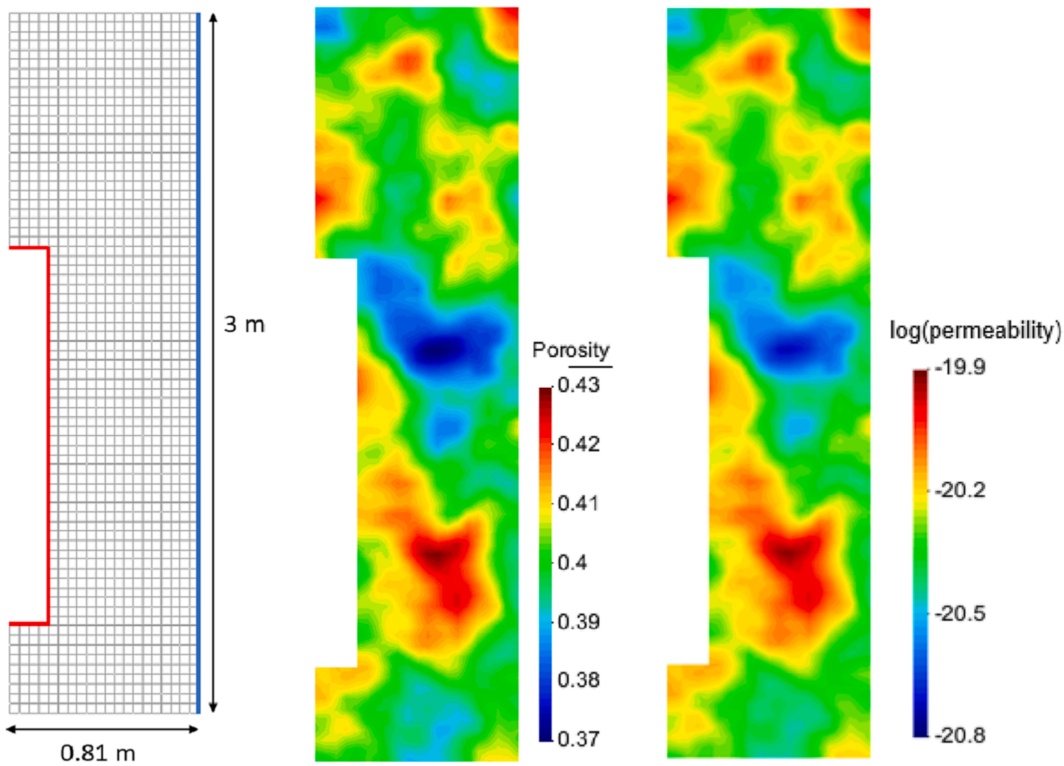

Fig. 22. Mock-up test. Model geometry (left), initial porosity (center), and initial permeability (right).

Table 5
Parameters of the mechanical constitutive model used in the analysis.

Elastic parameters	
κ_0	0.05
κ_{s0}	0.3
μ	0.4
α_{ss} : MPa	0
p_{ref} : MPa	0.01

Table 6
Hydraulic parameters used in the analysis.

Water retention curve (Van Genuchten with exponential law)		Intrinsic permeability (Exponential law)		Relative permeability (liquid)		Fick's law	
P_0 : MPa	20	k_0 : m^2	5×10^{-21}	n	3	τ	0.8
λ:	0.18	ϕ_0	0.4				
S_{ls}/S_{rl}:	1.0/0.01	b_k	30				
b_p	10						
ϕ_0	0.4						

Table 7
Thermal parameters used in the analysis.

Parameters	λ_s : Wm^{-1}K^{-1}	λ_l : Wm^{-1}K^{-1}	λ_g : Wm^{-1}K^{-1}
Value	2	0.6	0.05

lower than that, no spatial correlation is shown. If the range is $a = 0.1$m (Fig. 11 left), some correlation can be observed, in this case limited to a maximum of 5 elements in a given direction. If a higher range is considered (0.5m), as it is shown in Fig. 11 (right), the spatial correlation includes a larger area. Note that, given the dimensions of the model, a range of 0.5m corresponds to half the size of the model. Therefore, with smaller ranges the spatial correlation is limited to smaller areas of the model, even if the distributions of porosity are similar (Fig. 11 down). Since the distribution of porosity is heterogeneous, then the permeability of the matrix is also heterogeneous, as can be observed in Fig. 12 for the case of range $a = 0.5$m (Fig. 11 right), as well as many other variables, as explained above. Note that those distributions shown are the initial ones, since the distribution of porosity changes not only in space, but also in time.

5. Validation of the approach to model geomaterials with heterogeneous properties

The validation of the proposed approach is presented in this section by comparison with laboratory measurements from gas injection tests on compacted bentonite, carried out by the British Geological Survey. Details of the testing apparatus can be found in Daniels and Harrington (2017).

Using CODE_BRIGHT, a 3D coupled two-phase flow hydro-mechanical elastic model is considered, based in Damians et al. (2020). Damians et al. (2020) have modelled the experiment and have carried out a wide program of sensitivity calculations to investigate various aspects of the experiment and the clay material. In general, the geometry, boundary conditions and material parameters used are the same as in Damians et al. (2020), unless otherwise specified in this article. The main difference is that, in this case, a heterogeneous porosity field is generated with a mean porosity of 0.45 and a standard deviation of 0.033, which means a porosity range approximately between 0.35 and 0.55 (Fig. 13), with a range a = 0.04 m for spatial correlation, meanwhile in Damians et al. (2020) the porosity is considered constant and a heterogeneous permeability field is manually generated using different materials *ad hoc*.

In our model, the average initial intrinsic permeability k_0 is 3.3 $\times$ 10^{-21}m^2, matching the measurements of the experiment, and the change of the intrinsic permeability of the matrix with porosity has been modelled using the exponential law (Eq. (19)), with $b_k = 36$. Thus, due to the heterogeneous porosity field, initial intrinsic permeability of the matrix ranges between 1 $\times 10^{-22}$m^2 and 1 $\times$ 10^{-19}m^2, approximately. Moreover, capillary pressure changes with porosity according to Eq.

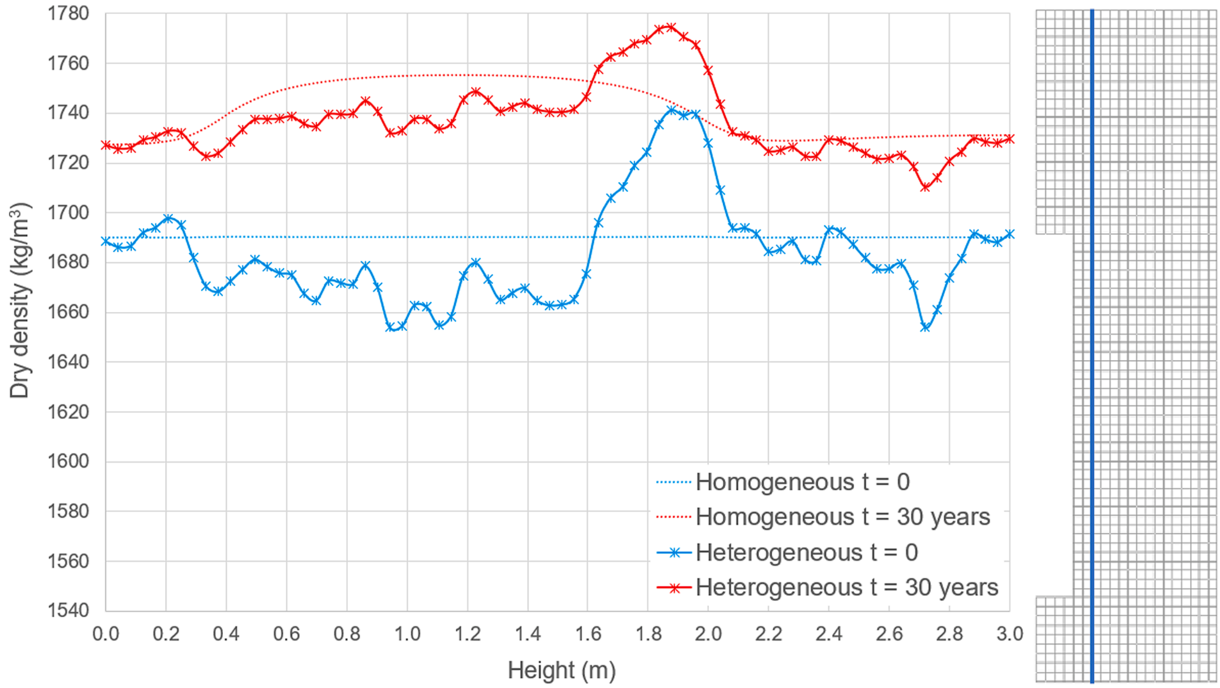

Fig. 23. Mock-up test. Dry density at t = 0 and t = 30 years for homogeneous and heterogeneous cases. Section near the heater.

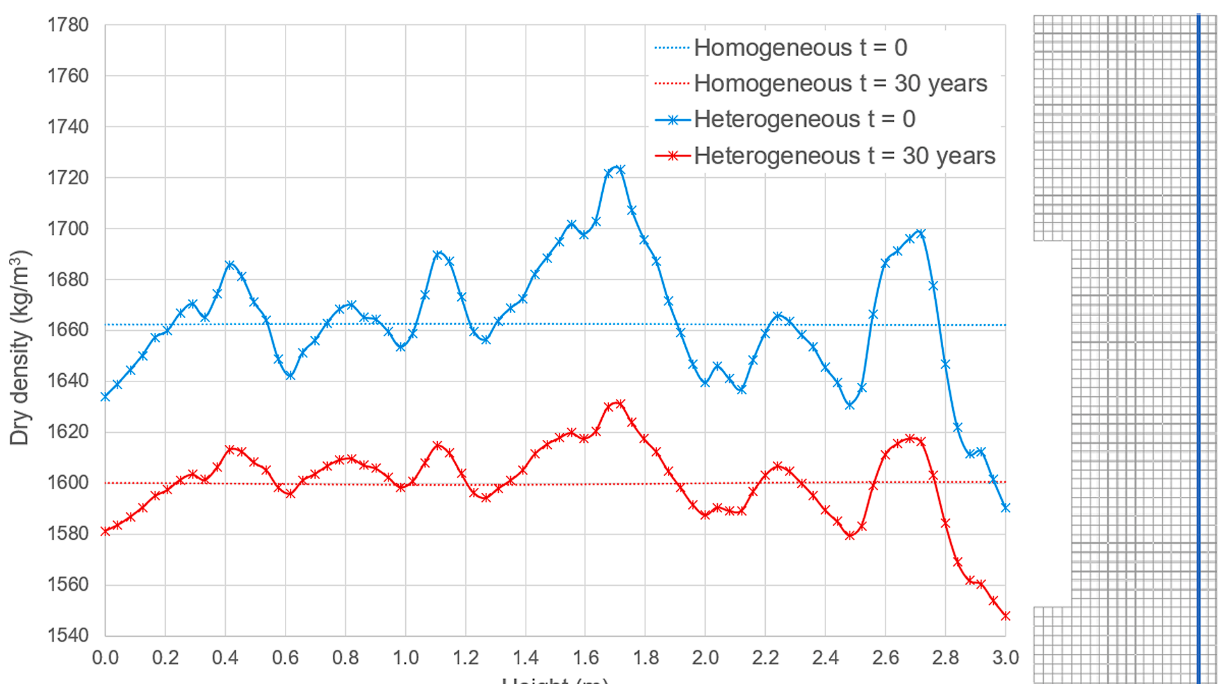

Fig. 24. Mock-up test. Dry density at t = 0 and t = 30 years for homogeneous and heterogeneous cases. Section near the hydration.

(22). This capillary pressure can also be attributed to the matrix. In addition, an embedded fracture model has been chosen (Eq. (16) and (18)) with the calibrated parameters shown in Table 2. Note that porosity does not change much during the experiment, due to material stiffness and constant volume test conditions. Therefore, the exponential law has an influence mainly in the initial intrinsic permeability, meanwhile the cubic law enhances the permeability in function of the strain locally developed.

Gas injection has different stages. Before day 46 the injection pressure is prescribed and after day 46 the flow rate is prescribed and, hence, gas pressure is calculated (Damians et al., 2020). Three heterogeneous identical models –with a different seed– have been run and the results are compared with the measurements and with a homogeneous case in which initial porosity is constant and equal to 0.45. The comparison (Fig. 14) shows the good correlation between the model and the experimental results, especially in the case of using the porosity distribution with seed = 2. Some variability depending on the seed is shown, particularly in terms of gas dissipation and less relevant concerning gas breakthrough pressure, which is slightly higher than in the experiment measurements. Besides the variability shown, a better matching

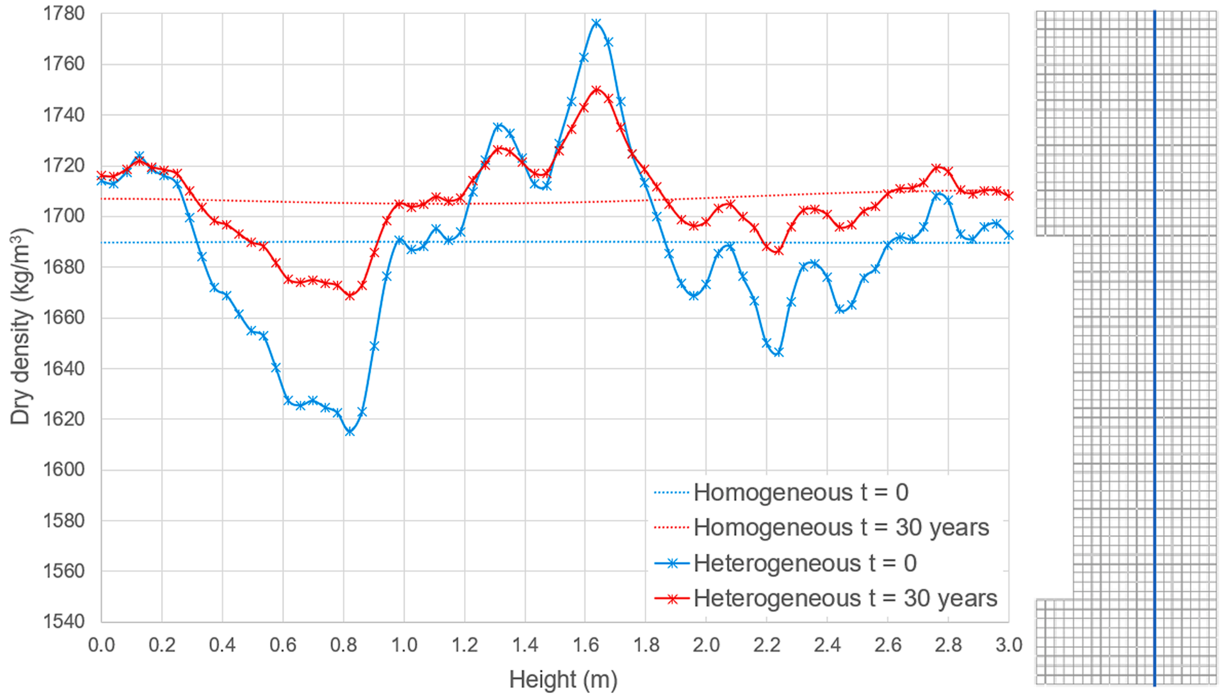

Fig. 25. Mock-up test. Dry density at t = 0 and t = 30 years for homogeneous and heterogeneous cases. Central section between the heater and the hydration.

compared to the homogeneous case is observed. An enhanced permeability gas path due to the aperture of discontinuities can be observed in the heterogeneous cases (Fig. 15), meanwhile in the homogeneous case the gas flows homogeneously through the sample. The heterogeneous case considered for this comparison has been the one with seed = 2.

Regarding the outflow, Fig. 16 shows the comparison between the heterogeneous and the homogeneous models and the measurements. It is observed that the results are not far from the measurements, although the peak in the outflow rate is not completely recovered. This could be due to the use of an elastic model (as in Damians et al., 2020). It is likely that considering inelastic deformations the results can get closer to the measurements, although this is beyond the scope of this validation exercise of the heterogeneous approach. Again, some variability can be observed among the three heterogeneous models, which seems to reproduce a slight peak that the homogeneous model is not able to reproduce.

Furthermore, plotting the gas volume being dissipated through the outflow side of the specimen, and comparing it with the measurements (Fig. 17), it can be observed that the total volume recovered according to the heterogeneous cases is in the range of the measured volume (specifically between seed 2 and 3 cases). This shows that the spatial distribution of the heterogeneity is relevant for the results obtained. On the other hand, the numerical models do not recover completely the gas volume increase rate observed around 70 days, which might be due to the fact that inelastic deformations are not considered, as stated above.

6. Other examples of the application of the heterogeneous model

In this section, two examples of application are presented to demonstrate the capabilities of the approach presented in modelling heterogeneous geomaterials. The first one is gas injection in a heterogeneous porous media, where special focus will be placed in the gas path. This problem is of special interest in various fields. Investigation has focussed on the gas flow migration with high-pressure gradients in low permeability media including the possibility of preferential paths development enhanced by deformations.

The second example is the effect of heterogeneity in a THM model being heat on one side and hydrated on the other side. This problem is motivated by the investigations on the behaviour of engineered barriers constructed with bentonite, which swells by hydration. A common idea is that swelling will close gaps (interfaces and contacts between blocks and boundaries). Nevertheless, this idea can be extended to the concept of material homogenization due to differential swelling, which depends on the clay density.

6.1. 2D gas injection test

An example of the proposed approach is presented here. Using CODE_BRIGHT, a 2D model with a discretised area of $1 \times 1\mathrm{m}^2$ is considered. A regular mesh of quadrilateral elements of dimensions $0.02 \times 0.02\mathrm{m}^2$ has been used (Fig. 10). Note that the generalised selective integration procedure, implemented in CODE_BRIGHT, can eliminate locking mesh and hour glassing issues of linear quadrilateral elements (Olivella et al., 1996). A small square at the lower left has been used to represent the area where gas is injected. Note that this example is THM, although the thermal part is negligible in this particular case and, hence, it can be performed as a HM model. Anyway, for that matter, the numerical cost of this example is extremely low.

The material has a mean porosity of 0.18 and a standard deviation of 0.002, which means a porosity range between 0.174 and 0.186, with a range $a = 0.5\mathrm{m}$ for spatial correlation. The average initial intrinsic permeability is $1 \times 10^{-20}\mathrm{m}^2$. Other relevant parameters are indicated in Table 3 and Table 4.

Regarding initial and boundary conditions, the initial stress is 12 MPa of compression, and 12 MPa of compression stress is applied as a boundary condition in the right and upper boundaries, meanwhile in the left and lower boundaries normal displacements are not allowed. The initial liquid pressure is 4.5 MPa and the initial gas pressure is 0.1 MPa, consistent with water exposed at atmospheric conditions. Same values of liquid and gas pressure are prescribed at the right and upper boundaries, meanwhile the right and lower boundaries are impermeable. The model is initially saturated with water.

Gas is injected in the lower left corner of the model at a progressively higher pressure, starting linearly from 0.1 MPa until 4.5 MPa after 100 h. After that, a gas flow is prescribed increasing linearly from 0 kg/s at

100 h until 5×10^{-7} kg/s at 200 h, and then the gas flow is maintained constant.

First, a homogeneous case has been modelled (Fig. 18). It can be observed that the gas propagates at a 45° angle from the injection point, due to the specific conditions of the model. However, if we introduce a slight heterogeneity, then we can observe that the gas path may be different (Fig. 19). In fact, in Fig. 19, different models have been performed using different spatially correlated heterogeneous distributions, but with the same average, variance and range. Then, the model has been performed under anisotropic heterogeneous fields of porosity with different angles of anisotropy. It can be observed that the gas tends to follow the direction of stratification (Fig. 20).

It can be observed that results may present significant differences among them and with respect to the homogeneous case, demonstrating that considering heterogeneous properties might be relevant in some cases.

Finally, Fig. 21 shows the evolution of gas injection pressure produced under different heterogeneous models and compared with the homogeneous case. The model is initially saturated with water. Note that after 100 h, gas is injected at a constant rate and the resulting pressure is calculated. The injection zone reaches nearly full gas saturation at nearly 500 h, which produces a temporary increase of the gas pressure. It can be observed that there is some variability in the gas pressure for the different cases. Thus, it could reproduce the variability that we can encounter in nature due to the heterogeneity of geomaterials.

6.2. Mock-up test

Another example of the proposed approach is presented here. The mock-up test, part of the FEBEX project (Gens et al., 2009; Rodriguez-Dono et al., 2018) consists of a cylindrical confining structure made of steel with an axial cylindrical electric heater and a clay barrier made of blocks of compacted bentonite, located between the confining structure and the heater. Using CODE_BRIGHT, a 2D axisymmetric model with a discretised area of radius 0.81m and a height of 3m is considered to model this test. A regular mesh of quadrilateral elements of dimensions approximately $0.04 \times 0.04\mathrm{m}^2$ has been used (Fig. 22). The problem is THM and the effect of gravity is not considered as suction is high and stresses are high, so gravity has little influence neither on the hydraulic problem nor on the mechanical.

The material has a mean porosity of 0.4 and a standard deviation of 0.01, which means a porosity range between 0.37 and 0.43, with a range $a = 0.5\mathrm{m}$ for spatial correlation. The average initial intrinsic permeability is $5 \times 10^{-21}\mathrm{m}^2$, ranging from $1.7 \times 10^{-21}\mathrm{m}^2$ to $1.4 \times 10^{-20}\mathrm{m}^2$ (Fig. 22). The initial conditions are 0.11 MPa of compressive stress, a suction of 105 MPa and 20 °C of temperature.

The mechanical thermo-elastoplastic model (Gens et al., 2009) has been considered. A swelling pressure dependent on porosity has been chosen for this example (Eq. (45)), with $c_0 = -1.741$, $c_1 = 4.117 \times 10^{-3}$ and $c_2 = -3.94 \times 10^{-7}$ (Fig. 8). Other relevant parameters are shown in Tables 5–7.

Regarding the mechanical boundary conditions, the normal displacements are not allowed in all boundaries during the test. Before the test starts, there is an initial hydration phase in the external boundary (blue line in Fig. 22 left), in which the mock-up is flooded with water and it is left during 10 days to allow the closure of the joints between blocks. Hence, suction is decreased progressively from 105 MPa in those 10 days in the external part of the model ($r = 0.81\mathrm{m}$), simulating an initial hydration of the bentonite. After this initial hydration, a constant water pressure is applied and the test starts (t = 0) applying heating power in the internal boundaries of the cylinder (red line in Fig. 22 left), to reach a temperature close to 100 °C. The aim is to observe the THM response of a bentonite barrier under the combined effects of outer hydration and inner heating.

The response of a homogeneous and a heterogeneous case is compared in Figs. 23–25, as well as the dry density profile at the beginning of the test (t = 0) and after 30 years. There are no other differences between the heterogeneous and the homogeneous model, except that the initial porosity is initially constant in the homogeneous case. Dry density profiles at three different radii are considered: one near the heater, one close to the hydration and one in the centre. It can be observed that the dry density profiles of the heterogeneous case reproduce closer values in average to the homogeneous one. However, in the heterogeneous case there is some variability, depending on the heterogeneous distribution taken. Nonetheless, unlike in the homogeneous case, note that the phenomenon of homogenization observed in reality (Gens et al., 2011; Sánchez et al., 2012) can be observed in the heterogeneous model, since the porosity variability is lower after 30 years than it is at t = 0. This phenomenon is especially clear at the central section (Fig. 25), where porosity is reduced at some points and increased at other locations, reducing the variability.

7. Summary and discussion

In this article, we present a new approach to perform THM calculations in a more realistic way by using information of the spatial distribution of density. The main idea in this approach is that an internal variable is used to develop a spatial variability, which acts as initial condition and in turn permits to calculate a spatial variability of other properties if dependence with porosity can be established. The internal variable is porosity, which can be calculated from dry density as it is better measured by image techniques.

The model has been validated showing a reasonable comparison with laboratory measurements. To illustrate some capabilities of the approach, we have shown that it can be relevant when modelling heterogeneous geomaterials. In particular, it has been demonstrated that the gas path in an in-situ gas injection test can be highly affected by a moderate heterogeneous distribution of porosity. In another application, a homogenization effect is shown when using a heterogeneous distribution of porosity in the hydration of a bentonite barrier, as well as variability on the dry density profile compared to the homogeneous case. These effects –we believe– could be relevant in different projects such as methane underground storage or CO_2 underground sequestration, fracking, geothermal, underground nuclear waste disposal, etc.

Therefore, the aim of the article is to provide a tool that may be useful in many THM cases to improve predictions or to provide a range of possible results by doing a handful of realizations with different distributions of porosity. The different distributions of porosity taken to perform the models can have the same or different mean or variance, and the same or different range for spatial correlation. Nonetheless, it is possible to use different distributions of porosity with the same mean, variance and range, just by changing the seed. Of course, some other parameters might also be considered heterogeneous, but for the moment, we have considered the ones described, for which dependence on porosity has been justified.

The current approach may be especially relevant when dealing with clay-based geomaterials (because porosity play a major role on various parameters), although it could also be relevant in other kind of porous geomaterials. Actually, when dealing with low porosity geomaterials (for instance crystalline rocks), the current approach based on porosity might need some adjustments like the introduction of some scaling factors or the introduction of other heterogeneous fields based on different variables, since porosity variation might not be the dominant factor to determine, for instance, the variations and spatial distributions of permeability, deformability or strength parameters like cohesion.

In future work, we will study the need for using different independent heterogeneous distribution for different parameters. In any case, one of the objectives of the paper is to reduce the amount of spatial information needed to characterize the heterogeneous behavior of the geomaterial while maintaining some coherence. Nonetheless, simple approaches have demonstrated to be very useful in engineering and research, making available for investigation relevant concepts that are not usually studied, following a broader modelling philosophy (Starfield and Cundall, 1988).

Finally, note that the influence of the heterogeneous porosity distribution in the thermal part has not been highlighted significantly in these examples (except for the THM calculation of Mock-up test), although we think it could be relevant in other applications (e.g. geothermal).

CRediT authorship contribution statement

Alfonso Rodriguez-Dono: Conceptualization, Methodology, Software, Writing – original draft. **Yunfeng Zhou:** Software, Writing – review & editing. **Sebastia Olivella:** Conceptualization, Methodology, Software, Writing – review & editing, Supervision.

Declaration of Competing Interest

The authors declare that they have no known competing financial interests or personal relationships that could have appeared to influence the work reported in this paper.

Data availability

The CODE_BRIGHT program can be downloaded from the official website: https://deca.upc.edu/en/projects/code_bright. Moreover, the source code as well as the examples contained in this article can be requested to the authors.

Acknowledgements

This research was supported by the CODE_BRIGHT Project (CIMNE, International Centre for Numerical Methods in Engineering) and by the DECOVALEX Project. The second author was supported by a CSC scholarship (No. 202008390058).

The CODE_BRIGHT project is funded by a Consortium composed by SKB (Sweden), Posiva (Finland), GRS (Germany) and ANDRA (France).

DECOVALEX is an international research project comprising participants from industry, government and academia, focusing on development of understanding, models and codes in complex coupled problems in sub-surface geological and engineering applications; DECOVALEX-2023 is the current phase of the project. The authors appreciate and thank the DECOVALEX-2023 Funding Organisations ANDRA, BASE, BGE, BGR, CAS, CNSC, COVRA, US DOE, ENRESA, ENSI, JAEA, KAERI, NWMO, NWS, SÚRAO, SSM and Taipower for their financial and technical support of the work described in this paper. The statements made in the paper are, however, solely those of the authors and do not necessarily reflect those of the Funding Organisations.

Special thanks to I.P. Damians for facilitating the original numerical model used in his work (Damians et al., 2020), in which one of the models presented in this article has been based.

References

Åkesson, M., Börgesson, L., Kristensson, O., 2010, SR-Site Data report. THM modelling of buffer, backfill and other system components.

Alabert, F., 1987. The practice of fast conditional simulations through the LU decomposition of the covariance matrix. Math. Geol. 19 (5), 369–386.

Alejano, L., Rodriguez-Dono, A., Alonso, E., Manín, G.-F., 2009. Ground reaction curves for tunnels excavated in different quality rock masses showing several types of post-failure behaviour. Tunn. Undergr. Space Technol. 24 (6), 689–705.

Alonso, E., Olivella, S., Pinyol, N., 2005. A review of Beliche Dam. Géotechnique 55 (4), 267–285.

Armand, G., Conil, N., Talandier, J., Seyedi, D.M., 2017. Fundamental aspects of the hydromechanical behaviour of Callovo-Oxfordian claystone: from experimental studies to model calibration and validation. Comput. Geotech. 85, 277–286.

Avar, B., Hudyma, N., Karakouzian, M., 2003. Porosity dependence of the elastic modulus of lithophysae-rich tuff: numerical and experimental investigations. Int. J. Rock Mech. Min. Sci. 40 (6), 919–928.

Bohling, G., 2005. Introduction to geostatistics and variogram analysis. Kansas Geol. Surv. 1, 1–20.

Börgesson, L., Johannesson, L.-E., Sanden, T., Hernelind, J., 1995, Modelling of the physical behaviour of water saturated clay barriers. Laboratory tests, material models and finite element application: Swedish Nuclear Fuel and Waste Management Co.

Brigaud, F., Vasseur, G., 1989. Mineralogy, porosity and fluid control on thermal conductivity of sedimentary rocks. Geophys. J. Int. 98 (3), 525–542.

Bürgmann, R., Pollard, D.D., Martel, S.J., 1994. Slip distributions on faults: effects of stress gradients, inelastic deformation, heterogeneous host-rock stiffness, and fault interaction. J. Struct. Geol. 16 (12), 1675–1690.

Coll, A., Ribó, R., Pasenau, M., Escolano, E., Perez, J. S., Melendo, A., Monros, A., Gárate, J., 2018. GiD v.14 User Manual.

Damians, I., Olivella, S., Gens, A., 2020. Modelling gas flow in clay materials incorporating material heterogeneity and embedded fractures. Int. J. Rock Mech. Min. Sci. 136, 104524.

Daniels, K.A., Harrington, J.F., 2017. The response of compact bentonite during a 1D gas flow test. British Geological Survey Open Report. Ref: OR/17/067.

Davis, M.W., 1987. Production of conditional simulations via the LU triangular decomposition of the covariance matrix. Math. Geol. 19 (2), 91–98.

Deutsch, C.V., Journel, A.G., 1992. Geostatistical Software Library and User's Guide, 8. Oxford University Press.

Dueck, A., 2004. Hydro-mechanical Properties of a Water Unsaturated Sodium Bentonite. Laboratory Study and Theoretical Interpretation. Lund University.

Emery, X., Lantuéjoul, C., 2006. Tbsim: A computer program for conditional simulation of three-dimensional Gaussian random fields via the turning bands method. Comput. Geosci. 32 (10), 1615–1628.

Firouzianbandpey, S., Griffiths, D.V., Ibsen, L.B., Andersen, L.V., 2014. Spatial correlation length of normalized cone data in sand: case study in the north of Denmark. Can. Geotech. J. 51 (8), 844–857.

Gens, A., Sánchez, M., Guimarães, L. d. N., Alonso, E., Lloret, A., Olivella, S., Villar, M., Huertas, F., 2009. A full-scale in situ heating test for high-level nuclear waste disposal: observations, analysis and interpretation. Géotechnique, 59(4), 377–399.

Gens, A., Olivella, S., 2001. THM phenomena in saturated and unsaturated porous media: fundamentals and formulation. Revue française de génie civil 5 (6), 693–717.

Gens, A., Vállejan, B., Sánchez, M., Imbert, C., Villar, M.V., Van Geet, M., 2011. Hydromechanical behaviour of a heterogeneous compacted soil: experimental observations and modelling. Géotechnique 61 (5), 367–386.

Géraud, Y., Yven, B., Sammartino, S., Homand, F., Villiéras, F., 2007. Mineralogy, texture and porosity of Callovo-Oxfordian argillites of the Meuse/Haute-Marne region (eastern Paris Basin). Mém. Soc. Géol. France 178, 73–90. ⟨hal-03698812⟩.

Gharti, H.N., Oye, V., Komatitsch, D., Tromp, J., 2012. Simulation of multistage excavation based on a 3D spectral-element method. Comput. Struct. 100, 54–69.

Han, D.-H., Nur, A., Morgan, D., 1986. Effects of porosity and clay content on wave velocities in sandstones. Geophysics 51 (11), 2093–2107.

Isaaks, E.H., Isaaks, D.A.E.S.E.H., Srivastava, R.M., Knovel, 1989, Applied Geostatistics. Oxford University Press.

Jorand, R., Vogt, C., Marquart, G., Clauser, C., 2013. Effective thermal conductivity of heterogeneous rocks from laboratory experiments and numerical modelling. J. Geophys. Res.: Solid Earth 118 (10), 5225–5235.

Journel, A.G., Huijbregts, C.J., 1976. Mining Geostatistics. Academic Press, London.

Karnland, O., Olsson, S., Nilsson, U., 2006. Mineralogy and Sealing Properties of Various Bentonites and Smectite-Rich Clay Materials. Swedish Nuclear Fuel and Waste Management Co.

Krishna, A.M., Katsumi, T., 2020. Geotechnics for Natural Disaster Mitigation and Management. Springer.

Lee, H.S., Cho, T.F., 2002. Hydraulic characteristics of rough fractures in linear flow under normal and shear load. Rock Mech. Rock Eng. 35 (4), 299–318.

Mahabadi, O., Randall, N., Zong, Z., Grasselli, G., 2012. A novel approach for micro-scale characterization and modeling of geomaterials incorporating actual material heterogeneity. Geophys. Res. Lett. 39 (1).

Mánica Malcom, M.Á., 2018. Analysis of underground excavations in argillaceous hard soils: weak rocks.

Matheron, G., 1973. The intrinsic random functions and their applications. Adv. Appl. Prob. 5 (3), 439–468.

Meier, P.M., Carrera, J., Sánchez-Vila, X., 1998. An evaluation of Jacob's method for the interpretation of pumping tests in heterogeneous formations. Water Resour. Res. 34 (5), 1011–1025.

Nishimura, S., Gens, A., Olivella, S., Jardine, R., 2009. THM-coupled finite element analysis of frozen soil: formulation and application. Géotechnique 59 (3), 159–171.

Olivella, S., 1995. Nonisothermal multiphase flow of brine and gas through saline media. Technical University of Catalonia [Ph.D].

Olivella, S., Alonso, E., 2008. Gas flow through clay barriers. Geotechnique 58 (3), 157–176.

Olivella, S., Vaunat, J., Rodriguez-Dono, A., 2022. CODE_BRIGHT User's Guide. Department of Civil and Environmental Engineering. Universitat Politècnica de Catalunya (UPC). https://deca.upc.edu/ca/el-departament/seccions/etcg/recerca/projectes/code_bright.

Olivella, S., Gens, A., Carrera, J., Alonso, E., 1996. Numerical formulation for a simulator (CODE_BRIGHT) for the coupled analysis of saline media. Eng. Comput. 13 (7), 87–112.

Olivella, S., Gens, A., 2002. A constitutive model for crushed salt. Int. J. Numer. Anal. Methods Geomech. 26 (7), 719–746.

Olivella, S., Gens, A., 2005. Double structure THM analyses of a heating test in a fractured tuff incorporating intrinsic permeability variations. Int. J. Rock Mech. Min. Sci. 42 (5–6), 667–679.
Oliver, M., Webster, R., 2014. A tutorial guide to geostatistics: computing and modelling variograms and kriging. Catena 113, 56–69.
Olsson, R., Barton, N., 2001. An improved model for hydromechanical coupling during shearing of rock joints. Int. J. Rock Mech. Min. Sci. 38 (3), 317–329.
Pakzad, R., Wang, S., Sloan, S., 2018. Numerical simulation of hydraulic fracturing in low-/high-permeability, quasi-brittle and heterogeneous rocks. Rock Mech. Rock Eng. 51 (4), 1153–1171.
Palchik, V., 1999. Influence of porosity and elastic modulus on uniaxial compressive strength in soft brittle porous sandstones. Rock Mech. Rock Eng. 32 (4), 303–309.
Palchik, V., Hatzor, Y.H., 2002. Crack damage stress as a composite function of porosity and elastic matrix stiffness in dolomites and limestones. Eng. Geol. 63 (3–4), 233–245.
Popov, Y., Beardsmore, G., Clauser, C., Roy, S., 2016. ISRM suggested methods for determining thermal properties of rocks from laboratory tests at atmospheric pressure. Rock Mech. Rock Eng. 49 (10), 4179–4207.
Rodriguez-Dono, A., Olivella, S., Mokni, N., 2018. Assessment of a high-level spent nuclear fuel disposal model. Environ. Geotech. 7 (1), 42–58. https://doi.org/10.1680/jenge.18.00017.
Rybacki, E., Reinicke, A., Meier, T., Makasi, M., Dresen, G., 2015. What controls the mechanical properties of shale rocks?–Part I: strength and Young's modulus. J. Pet. Sci. Eng. 135, 702–722.
Sammartino, S., Siitari-Kauppi, M., Meunier, A., Sardini, P., Bouchet, A., Tevissen, E., 2002. An imaging method for the porosity of sedimentary rocks: adjustment of the PMMA method—example of a characterization of a calcareous shale. J. Sediment. Res. 72 (6), 937–943.
Sánchez, M., Gens, A., Olivella, S., 2012. THM analysis of a large-scale heating test incorporating material fabric changes. Int. J. Numer. Anal. Meth. Geomech. 36 (4), 391–421.
Song, Y., Davy, C.A., Troadec, D., Blanchenet, A.-M., Skoczylas, F., Talandier, J., Robinet, J.-C., 2015. Multi-scale pore structure of COx claystone: towards the prediction of fluid transport. Mar. Pet. Geol. 65, 63–82.
Song, F., Rodriguez-Dono, A., 2021. Numerical solutions for tunnels excavated in strain-softening rock masses considering a combined support system. App. Math. Model. 92, 905–930.
Song, F., Rodriguez-Dono, A., Olivella, S., Zhong, Z., 2020. Analysis and modelling of longitudinal deformation profiles of tunnels excavated in strain-softening time-dependent rock masses. Comput. Geotech. 125, 103643.
Song, F., Rodriguez-Dono, A., Olivella, S., 2021. Hydro-mechanical modelling and analysis of multi-stage tunnel excavations using a smoothed excavation method. Comput. Geotech. 135, 104150.
Starfield, A.M., Cundall, P.A., 1988. Towards a methodology for rock mechanics modelling. Int. J. Rock Mech. Min. Sci. Geom. Abstr. 25 (3), 99–106.
Tamayo-Mas, E., Harrington, J.F., Brüning, T., Wang, J., Carson, J.K., North, M.F., Cleland, D.J., 2006. A new approach to modelling the effective thermal conductivity of heterogeneous materials. Int. J. Heat Mass Transf. 49(17–18) 3075–3083.
Tan, C.T., Homsy, G.M., 1992. Viscous fingering with permeability heterogeneity. Phys. Fluids A: Fluid Dyn. 4 (6), 1099–1101.
Toprak, E., Olivella, S., Pintado, X., 2018. Modelling engineered barriers for spent nuclear fuel repository using a double-structure model for pellets. Environ. Geotech. https://doi.org/10.1680/jenge.17.00086.
Trabelsi, H., Jamei, M., Zenzri, H., Olivella, S., 2012. Crack patterns in clayey soils: Experiments and modelling. Int. J. Numer. Anal. Methods Geomech. 36 (11), 1410–1433.
Van Genuchten, M.T., 1980. A closed-form equation for predicting the hydraulic conductivity of unsaturated soils. Soil Sci. Soc. Am. (SSSA) J. 44 (5), 892–898. https://doi.org/10.2136/sssaj1980.03615995004400050002x.
Wu, K., Nunan, N., Crawford, J.W., Young, I.M., Ritz, K., 2004. An efficient markov chain model for the simulation of heterogeneous soil structure. Soil Sci. Soc. Am. J., 68, 346–351. doi: 10.2136/sssaj2004.3460.
Wu, Y., Liu, J., Elsworth, D., Miao, X., Mao, X., 2010. Development of anisotropic permeability during coalbed methane production. J. Nat. Gas Sci. Eng. 2 (4), 197–210.
Yu, C., Ji, S., Li, Q., 2016. Effects of porosity on seismic velocities, elastic moduli and Poisson's ratios of solid materials and rocks. J. Rock Mech. Geotech. Eng. 8 (1), 35–49.
Yven, B., Sanmartino, S., Geraud, Y., Homand, F., Villieras, F., 2007. Mineralogy, texture and porosity of Callovo-Oxfordian argillites of the Meuse/Haute-Marne region (eastern Paris Basin). Mém. Soc. géol. France, n.s. 178, 73–90.
Zienkiewicz, O.C., Taylor, R.L., 2000. The Finite Element Method: Solid Mechanics. Butterworth-Heinemann.
Zienkiewicz, O.C., Taylor, R.L., 2005. The Finite Element Method for Solid and Structural Mechanics. Elsevier.